

Accepted Manuscript

Hydrogen-enhanced-plasticity mediated decohesion for hydrogen-induced intergranular and “quasi-cleavage” fracture of lath martensitic steels

Akihide Nagao , Mohsen Dadfarnia , Brian P. Somerday ,
Petros Sofronis , Robert O. Ritchie

PII: S0022-5096(17)30781-0
DOI: [10.1016/j.jmps.2017.12.016](https://doi.org/10.1016/j.jmps.2017.12.016)
Reference: MPS 3258



To appear in: *Journal of the Mechanics and Physics of Solids*

Received date: 4 September 2017
Revised date: 30 December 2017
Accepted date: 31 December 2017

Please cite this article as: Akihide Nagao , Mohsen Dadfarnia , Brian P. Somerday , Petros Sofronis , Robert O. Ritchie , Hydrogen-enhanced-plasticity mediated decohesion for hydrogen-induced intergranular and “quasi-cleavage” fracture of lath martensitic steels, *Journal of the Mechanics and Physics of Solids* (2018), doi: [10.1016/j.jmps.2017.12.016](https://doi.org/10.1016/j.jmps.2017.12.016)

This is a PDF file of an unedited manuscript that has been accepted for publication. As a service to our customers we are providing this early version of the manuscript. The manuscript will undergo copyediting, typesetting, and review of the resulting proof before it is published in its final form. Please note that during the production process errors may be discovered which could affect the content, and all legal disclaimers that apply to the journal pertain.

Hydrogen-enhanced-plasticity mediated decohesion for hydrogen-induced intergranular and “quasi-cleavage” fracture of lath martensitic steels

Akihide Nagao ^{a,b,c}, Mohsen Dadfarnia ^{a,b}, Brian P. Somerday ^{a,d}, Petros Sofronis ^{a,b},
Robert O. Ritchie ^{a,e,*}

^a International Institute for Carbon Neutral Energy Research (WPI-I2CNER), Kyushu University,
744 Moto-oka, Nishi-ku, Fukuoka 819-0395, Japan

^b Department of Mechanical Science and Engineering, University of Illinois at Urbana-Champaign,
1206 W. Green St., Urbana, IL 61801, USA

^c Material Surface & Interface Science Research Department, Steel Research Laboratory, JFE Steel
Corporation,
1-1 Minamiwatarida-cho, Kawasaki-ku, Kawasaki, Kanagawa 210-0855, Japan

^d Southwest Research Institute,
San Antonio, TX 78240, USA

^e Materials Sciences Division, Lawrence Berkeley National Laboratory, and Department of Materials Science
and Engineering, University of California, Berkeley, CA 94720, USA

E-mail address: a-nagao@jfe-steel.co.jp (A. Nagao).
dadfarni@illinois.edu (M. Dadfarnia).
brian.somerday@swri.org (B.P. Somerday).
sofronis@illinois.edu (P. Sofronis).
roritchie@lbl.gov (R.O. Ritchie).

December 29, 2017

* Corresponding author: roritchie@lbl.gov

Abstract

Hydrogen embrittlement of lath martensitic steels is characterized by intergranular and “quasi-cleavage” transgranular fracture. Recent transmission electron microscopy (TEM) analyses (Nagao *et al.*, 2012a, 2014a, 2014b, 2014c) of samples lifted from beneath fracture surfaces through focused ion beam machining (FIB) revealed a failure mechanism that can be termed *hydrogen-enhanced-plasticity mediated decohesion*. Fracture occurs by the synergistic action of the hydrogen-enhanced localized plasticity and decohesion. In particular, intergranular cracking takes place by dislocation pile-ups impinging on prior austenite grain boundaries and quasi-cleavage is the case when dislocation pile-ups impinge on block boundaries. These high-angle boundaries, which have already weakened by the presence of hydrogen, debond by the pile-up stresses. The micromechanical model of Novak *et al.* (2010) is used to quantitatively describe and predict the hydrogen-induced failure of these steels. The model predictions verify that introduction of nanosized (Ti,Mo)C precipitates in the steel microstructure enhances the resistance to hydrogen embrittlement. The results are used to discuss microstructural designs that are less susceptible to hydrogen-induced failure in systems with fixed hydrogen content (closed systems).

Keywords: Hydrogen embrittlement; martensitic steels; plasticity; decohesion; weakest link statistics

1. Introduction

Novak *et al.* (2010) advanced a physical-based statistical micro-mechanical model of hydrogen embrittlement of a high-strength low-alloy steel manifested by intergranular cracking. According to the model, hydrogen-induced fracture is a result of the synergistic action of the hydrogen-enhanced localized plasticity (HELP) (Beachem 1972; Birnbaum *et al.*, 1997; Robertson, 1999; Robertson *et al.*, 2009; Nagao *et al.*, 2015) and hydrogen-enhanced decohesion (HEDE) (Troiano, 1960; Oriani and Josephic 1977; Oriani, 1987; Gerberich *et al.*, 1996) mechanisms. Specifically, hydrogen trapped at dislocations decreases the separation distance between dislocations in pile-ups, thus accentuating the stress at the tip of the pile-ups; upon

impinging on grain-boundary carbides, this in turn modifies the carbide/matrix interface strength with the hydrogen that is deposited by the dislocations at the interface, which in concert with the locally elevated stress produces intergranular decohesion. The quantitative aspects of the model are based on the interplay of locally enhanced hydrogen concentrations, plastic straining for hydrogen trapping, and local stress, the combination of which determines the “weakest-link” for the local decohesion event to initiate. In other words, the local failure probability is a complex interaction between stress that debonds an interface and local hydrogen coverage promoted by dislocation pile-ups that weaken the interface. In this work, we employ the model of Novak *et al.* (2010): i) to quantify the hydrogen-induced intergranular and “quasi-cleavage” transgranular cracking in lath martensitic steels in which our experiments indicate that the fracture process/event is mediated by plasticity, and ii) to quantify the resistance of lath martensitic steels with nanosized (Ti,Mo)C precipitates to hydrogen embrittlement.

High-strength lath martensitic steels are widely utilized in various structures and components for their excellent combination of strength and toughness. It is well recognized, however, that the presence of hydrogen in these steels can lead to sudden and unexpected catastrophic fracture, which commonly results from intergranular and/or “quasi-cleavage” transgranular cracking. Due to this hydrogen embrittlement, the tensile strength of lath martensitic steels for practical use has been limited to the range from 1000 to 1200 MPa and for environments in which hydrogen uptake is not severe (Gangloff and Somerday, 2012; Takai and Akiyama, 2012; Somerday and Sofronis, 2014). In the following, the literature on the hydrogen effect on the failure of lath martensitic steels is reviewed and it is deduced that the most recent experimental results of Nagao *et al.* (2012a, 2014a, 2014b, 2014c) argue for the applicability of the model of Novak *et al.* (2010) for fracture prognosis of lath martensitic steels.

Hydrogen-induced intergranular failure along prior austenite grain boundaries in lath martensitic steels was first explained by the HEDE mechanism. Using a modified wedge opening load (WOL) specimen, Oriani and Josephic (1974; 1977) determined threshold pressures of hydrogen gas necessary to cause crack propagation in an AISI 4340 lath martensitic steel, with 1700 MPa yield strength, as a function of applied stress-intensity factor. The authors claimed that the intergranular features at low stress intensities and the plastic tearing at high stress intensities

were attributed to hydrogen-induced decohesion. However, the authors did not offer any rational explanation for this claim based on the understanding of the microstructural features of deformation. Yoshino and McMahon (1974) studied the effect of hydrogen and cohesion-lowering segregants, such as phosphorous, manganese and silicon, on the resistance to hydrogen embrittlement of an HY 130 lath martensitic steel, with 959 MPa yield strength, using edge-notched and pre-cracked cantilever-bend specimens. In the embrittled condition after step-cooling whereby the cohesion-lowering elements segregate to prior austenite grain boundaries, the steel was found to be highly susceptible to intergranular crack growth in the presence of hydrogen, whereas the same steel in the unembrittled condition without step-cooling was much less sensitive to hydrogen. A similar result was also obtained by the same research group (Bandyopadhyay *et al.*, 1983) with an AISI 4340 lath martensitic steel of higher yield strength of 1200-1900 MPa. Based on these observations, McMahon and co-workers concluded that intergranular fracture is a result of the synergistic action of hydrogen and the other metalloid impurities in reducing grain boundary cohesion. Gerberich *et al.* (1988) examined the effect of hydrogen on stage II crack-growth rates in AISI 4340 lath martensitic steels with 1340 and 1620 MPa yield strengths. They conducted sustained-load tests using standard compact-tension specimens at various temperatures between -43° and 146°C . In the 1340 MPa yield strength steel, hydrogen was trapped at oxysulfide particles with a binding energy ~ 75 kJ/mol; where these particles intersect prior austenite grain boundaries, trapped hydrogen promotes ductile fingers of intergranular fracture which later triggers tearing of $100\text{ }\mu\text{m}$ size ligaments by microvoid coalescence. For the 1620 MPa yield strength steel, conversely, hydrogen was trapped along lath intersections with prior austenite grain boundaries with a binding energy ~ 27 kJ/mol; this promotes $\sim 1\text{ }\mu\text{m}$ size striations along intergranular facets. In both cases, the fractography was consistent with the proposed model of hydrostatic-stress qualified hydrogen concentration in the lattice, enhanced concentrations at trap sites where fracture nucleates, and local and discontinuous fracture instabilities promoted by the HEDE mechanism.

Investigating hydrogen-induced intergranular failure along prior austenite grain boundaries, Lynch (1984) compared fracture surfaces produced in hydrogen gas and liquid mercury using a series of D6AC lath martensitic steels with hardness varying from HV30 ~ 340 to ~ 640 . Lynch

performed three-point bend tests and examined the fracture surfaces by scanning electron (SEM) and transmission electron microscopy (TEM); germanium-shadowed, secondary-carbon replicas were used for the TEM study. The intergranular facets generated in hydrogen gas exhibited areas of dimples, tear ridges, and smooth areas when examined by SEM. Interestingly, stereoscopic viewing of TEM micrographs revealed small depressions in areas that appeared smooth using SEM for the 400°C tempered condition. For the 650°C tempered condition, SEM and TEM studies revealed that intergranular fractures were covered by well-defined dimples. From these observations and fractographic similarities between hydrogen embrittlement and liquid-metal embrittlement, Lynch proposed that an adsorption-induced reduction in the strength of interatomic bonds at crack tips is the underlying cause for this intergranular failure process. Nagumo and Matsuda (2002) examined the effect of hydrogen on intergranular fracture of lath martensitic steels, with tensile strengths from 1240 to 1260 MPa and differing manganese contents from 0.47 to 1.42 mass%. These authors conducted tensile tests at a strain rate of 5.6×10^{-6} /s under concurrent cathodic hydrogen charging and found pronounced degradation of the tensile properties with increasing manganese content. The fracture mode remained intergranular with tear traces along lath boundaries, although these tear traces were less frequently observed, coupled with an average decrease in surface roughness, with increasing manganese content. The authors proposed that the primary function of hydrogen in intergranular fracture is to stabilize and increase the density of strain-induced vacancies that lead to the formation of microcracks or microvoids in the vicinity of the boundaries.

The presence of ductile fingers, dimples, tear ridges, small depressions and tear traces on the hydrogen-induced intergranular fracture surfaces of lath martensitic steels revealed by the studies of Gerberich *et al.* (1988), Lynch (1984), and Nagumo and Matsuda (2002) suggests that plasticity is involved in the hydrogen-induced intergranular failure of lath martensitic steels. In their seminal work, Jokl *et al.* (1980) explained that brittle fracture of deformable solids is always accompanied by plastic processes and related the attendant plastic work to the reversible work of decohesion quantitatively. Thus, hydrogen and metalloid impurities, by reducing the reversible work of interfacial separation, also indirectly reduce the associated plastic work to cause brittle fracture. More recently, Nagao *et al.* (2012a, 2014a, 2014b) studied the role of

hydrogen in the intergranular fracture of a lath martensitic steel with 0.2% proof stress of 1290 MPa. Using FIB machining, they extracted thin samples from underneath the fracture surface and examined the microstructure developed immediately beneath the fracture surface in a transmission electron microscope. These TEM microscopic observations revealed intense slip banding (deformation bands) while the lath boundaries were so disturbed by the severe plastic straining that they were difficult to discern. This microstructure discovered by Nagao *et al.* (2012a, 2014a, 2014b) provides clearer and more direct evidence of the involvement of plasticity in the hydrogen-induced intergranular fracture.

Fracture prognosis for lath martensitic steels operating in hydrogen is not available as of yet partly due to the lack of precise identification of the basic microscopic mechanisms that precede the intergranular fracture event and partly due to the complex grain-boundary morphology of these steels that consists of a four-level hierarchy: prior austenite grain, packet, block, and lath boundaries. Prompted by the recent results of Nagao *et al.* (2012a, 2014a, 2014b), we apply the model of Novak *et al.* (2010) to macroscopically quantify the hydrogen embrittlement of lath martensitic steels that is manifested by intergranular and “quasi-cleavage” transgranular failure microscopically. Two types of tempered lath martensitic steels were used in this study: Ti-free baseline and Ti-added steels. These steels are modified variations of an AISI 4140 steel and could be used for various industrial applications such as bolts, gears and shafts. An important goal of this work is to also assess the resistance to hydrogen embrittlement of the Ti-added steels in which additional hydrogen trap sites at nanosized (Ti,Mo)C precipitates are present.

2. Experimental procedures

2.1 Materials

Ti-free and Ti-added medium carbon high-strength tempered lath martensitic steels were used in the present study; chemical compositions along with the calculated A_{c1} (Andrews, 1965), A_{r3} (Ouchi *et al.*, 1982) and M_s (Krauss, 1990) transformation temperatures are given in Table 1. The Ti-free baseline steel is a modified AISI 4140 steel with Cr removed and Mn content raised to adjust its hardenability; for ease of reference; this will be referred to as steel A. The Ti-added steel had a Ti/C atomic ratio of 1/39; this will be referred to as steel B. The levels of P and S in

both steels were intentionally reduced to minimize their sensitivity to hydrogen embrittlement.

A schematic summary of the rolling and heat treatment is presented in Fig. 1. After being austenitized at 1230°C for 120 min, the slabs were rolled in the recrystallization region between 1150° and 1110°C followed by rolling in the non-recrystallization region between 800° and 780°C to 20 mm-thick plates. All Ti carbide particles were estimated to have dissolved in the matrix during austenization at 1230°C (Narita, 1975). The steel plates were processed by modified ausforming with a rolling reduction ratio in the non-recrystallization region of 50% (Nagao *et al.*, 2012b). To obtain a full lath martensite structure, the steel plates were direct-quenched from 700° to 7°C using a water spray with the average cooling rate 42°C /s. The steel plates were subsequently subjected to a sub-zero treatment by immersion in liquid nitrogen to promote the transformation of any retained austenite to martensite. Finally, the quenched plates were tempered in an atmospheric furnace to improve elongation and toughness through dislocation rearrangement/annihilation, substructure recovery, and precipitation of cementite particles and/or Ti carbide precipitates. The Ti-free baseline steel A plates were heated to the temperature of either 500°C at a rate of 0.4°C /s or 550°C at a rate of 0.5°C /s or 550°C at a rate of 1.9°C /s, removed from the furnace immediately on reaching the tempering temperature, and cooled in air at an average rate of 0.1-0.2°C /s. To mark these Ti-free baseline steels for their tempering condition, they will be referred to as steels A500, A550 α and A550 β , respectively. The Ti-added steel B plates, on the other hand, were heated at a rate 0.5 – 0.7°C /s and tempered at 500° (steel B500), 550° (steel B550) or 600 °C (steel B600) for 60 min to produce nanosized Ti carbide precipitates, and cooled in air at 0.1 – 0.3°C /s. The principal axes of these plates are defined as follows: the axes parallel and transverse to the rolling direction are defined as RD and TD, respectively, and the one normal to them as ND.

2.2 Materials characterization

The undeformed microstructure in the RD-ND plane at the quarter thickness section of the steel plates was determined by a combination of optical microscopy (OM), SEM, electron backscatter diffraction (EBSD) and TEM. To reveal the microstructure for the OM study, the surface of the samples was etched with 3% Nital or picric acid. A Zeiss Supra 40VP scanning

electron microscope equipped with an EDAX/TSL Hikari high-speed EBSD detector was used for the EBSD analysis at 20 keV to determine packet and block boundaries. The microstructure was further assessed using a Philips CM20 field-emission transmission electron microscope operating at 200 keV to reveal lath boundaries, dislocation structures and cementite particles. Thin foil specimens were prepared for the TEM observations. Further, the microstructure etched with 3% Nital was observed with a Hitachi S-4000 field-emission scanning electron microscope operating at an accelerating voltage of 15 keV to identify cementite particles and inclusions. As for the steels B500, B550 and B600, nanosized Ti carbide precipitates were observed in the Philips CM20 field-emission transmission electron microscope operating at 200 keV. The scanning electron microscope and the transmission electron microscope were both equipped with an energy dispersive x-ray (EDX) unit.

To quantify the amount of nanosized Ti carbide precipitates, steels B500, B550 and B600 were subjected to an extracted residue analysis. An electrolytically extracted sample in methanol solution that contained 10 vol.% acetylacetone and 1 mass% tetramethylammonium chloride was analyzed with an inductively coupled plasma-mass spectrometer (ICP) to determine the amount of titanium as carbide and nitride and also molybdenum as carbide. The electrolyte solution was subsequently analyzed by inductively coupled plasma-mass spectrometry (ICP-MS) to quantify the amount of titanium as solute. Further, dissoluble extracts in methanol solution containing 10 vol.% bromine were analyzed by a bis-pyrazolon method to determine the amount of titanium as nitride.

The dislocation density in steel B550 was experimentally determined as a function of plastic strain. A uniaxial tension test was performed in accordance with ASTM Standard E-8 using a subsize specimen at a constant cross-head speed of 8.0 $\mu\text{m/s}$ at room temperature. A sheet-type specimen with reduced section dimensions of 1.5 (ND) x 6.0 (TD) x 32.0 (RD) mm was machined on a milling machine from the surface portion of the steel plate, polished with emery paper and buff-polished using an alumina slurry. Vickers indents were generated under 9.8 N load in a line at 5 mm spacing in the center of the width of the specimen on 12 points intentionally including the grip sections. The length of the spacing between the indents was measured before and after the tension test and the average strain was computed for each of the 11

spacings. After the tension test, x-ray diffraction (XRD) measurements were conducted on selected 5 points of various strains between 0.0% and 28.3%. The diffraction lines were recorded to cover the diffractions of (110), (211), and (220) in order to determine the XRD peak width, β_m deg. The instrumental peak width, β_s deg, was also measured with NIST silicon standards; the corrected peak width, β deg, was computed using $\beta = \sqrt{\beta_m^2 - \beta_s^2}$. These data were analyzed using the Williamson-Hall equation:

$$\beta \frac{\cos \theta}{\lambda} = \frac{0.9}{D} + 2\varepsilon \frac{\sin \theta}{\lambda}, \quad (1)$$

where θ is the diffraction angle, λ the x-ray wave-length, D the average particle size, and ε the strain (Williamson and Hall, 1953). Subsequently, the dislocation density, ρ , was calculated through $\rho = 14.4(\varepsilon/b)^2$, where $b = 0.248$ nm is the Burgers vector (Williamson and Smallman, 1956). A Rigaku RINT-RAPID II system with CoK_α radiation was used for the XRD measurements.

2.3. Mechanical tests

Uniaxial tension tests of the uncharged A500, A550 α , A550 β , B500, B550, and B600 steels were performed in accordance with ASTM Standard E-8 using small-size specimens, of diameter of 4.0 mm, at a constant cross-head speed of 0.5 $\mu\text{m/s}$ at room temperature. Round-type specimens with reduced section dimensions of 4.0 (diameter) x 20.0 (RD) mm were machined on a lathe from the steel plates, with the center of the specimens at the quarter thickness portion of the plates.

To study the hydrogen effect, precharged single-notched bend (SE(B)) specimens of the A500, A550 α , A550 β , B500, B550 and B600 steels were tested in four-point bending. The specimens that were machined using an electric discharge machine from the quarter thickness section of the steel plates, were 6.35 mm thick in the ND direction, 12.7 mm wide in the TD direction, and 101.6 mm long in the RD direction. The uncracked ligament was 8.47 mm, the notch angle was 22.5 deg with a root radius of 0.25 mm. These dimensions and notch angle are exactly the same as those of the specimens used in the experiments by Novak *et al.* (2010). A

schematic illustration of the bend specimen is shown in Fig. 2.

To prevent egress of hydrogen during cooling, depressurization of the autoclave, and testing, an 18 μm -thick zinc layer was deposited on the bend specimens as well as on reference small blocks of steels (20.0 (ND) x 10.0 (TD) x 10.0 (RD) mm) that were used in the thermal desorption analysis (TDA) to determine the trap states, the binding energy, and the hydrogen content. The electroplating was performed in an aqueous solution containing ammonium chloride and zinc chloride at a current density of 28.00 mA/cm^2 for 28 min at 25°C; see Nagao *et al.* (2012b) for details. Following the zinc-electroplating, the specimens were baked in a vacuum furnace at 150°C for 24 h to remove any hydrogen introduced during electroplating. The zinc-electroplated specimens were subsequently charged with hydrogen in an autoclave filled with high-pressure hydrogen gas at 250°C for 21 days under gas pressure of either 31 or 138 MPa. Some uncharged zinc-electroplated specimens were also used for testing.

One advantage of thermal precharging in hydrogen gas over other hydrogen exposure (*e.g.*, electrochemical) methods is that one can easily apply thermodynamic relationships to calculate hydrogen concentration and distribution in the material. For example, the concentration of hydrogen in the lattice, C_L , can be readily calculated from Sieverts law (*i.e.*, $C_L = K\sqrt{f}$, where K is solubility and f is fugacity), such that the hydrogen fugacity is easily determined from the measured pressure. The concentration of hydrogen in trap sites can also be calculated, provided that the trap binding energies and trap site densities are known.

At the end of the 21-day hydrogen charging period, hydrogen residing at normal interstitial lattice sites (NILS) was assumed to be in equilibrium with hydrogen gas, as dictated by Sieverts law, and consequently the hydrogen concentration was uniform throughout the specimens. Using round-type specimens machined from a tempered lath martensitic steel with 1238 MPa tensile strength, Nagao *et al.* (2012b), independently verified that the zinc-electroplating functions as a perfect internal hydrogen insulator even under stress of magnitude equal to 90% of the specimen tensile strength for at least 216 h. In the present study, the longest loading period of the SE(B) specimens was 5.2 h; hence, it is safe to assume that no hydrogen outgassed from the specimens by the end of loading.

The uncharged and 31/138 MPa hydrogen-charged A500, A550 β , B500 and B550 steel specimens were subjected to four-point bending at an extremely slow displacement rate of 0.1 $\mu\text{m/s}$ at room temperature in order to allow for internal hydrogen redistribution during testing. The results are presented in terms of the nominal bending stress, σ_{nom} , which denotes the maximum bending stress in a straight beam of height a , and is computed through $\sigma_{nom} = 6Fz / Ba^2$, where F is the applied force, z is the length of the moment arm, B is the thickness of the bend specimen and a is the uncracked ligament. The fracture surfaces were examined with a JEOL 6060LV scanning electron microscope operating at an accelerating voltage of 15 keV.

The hydrogen content of the uncharged and 31/138 MPa hydrogen-charged A500, A550 β , B500 and B550 steel blocks was determined by means of gas chromatograph thermal desorption analysis (GC-TDA). Immediately before the GC-TDA test, the zinc-electroplating was removed from the blocks by grinding the specimen on a wheel with #240 SiC paper. Each block was heated at a constant rate of 200°C /h from room temperature to 550°C to evolve the hydrogen in a controlled manner. The measured hydrogen content was used as initial condition for the numerical simulations reported in Sections 4 and 5.

Following Novak *et al.* (2010), we tested A550 α steel SE(B) specimens both in the uncharged and the 138 MPa hydrogen-charged condition at a displacement rate of 0.1 $\mu\text{m/s}$ and room temperature to identify the critical local fracture events/processes. The tests were interrupted as soon as the maximum load was reached, which coincides with the onset of fracture, and the area in the vicinity of the unbroken notch root was examined in a JEOL 6060LV scanning electron microscope operating at an accelerating voltage of 15 keV to discern the location of the initial fracture event in order to ascertain whether the fracture is locally stress- or strain-controlled.

Lastly, Novak *et al.* (2010) argued that loading the SE(B) specimen by a macroscopic displacement rate of 0.1 $\mu\text{m/s}$ produces a local plastic strain rate at the notch root that does not exceed 10^{-4} /s. A strain rate of this order of magnitude is, therefore, slow enough for plasticity-mediated hydrogen embrittlement to operate (Birnbaum and Sofronis, 1994). To confirm this, we investigated the effect of the strain rate with the uncharged and the 138 MPa hydrogen-charged

steel B600 SE(B) specimens by increasing the displacement rate from 0.1 to 1.0 and 10.0 $\mu\text{m/s}$.

The results of all mechanical four-point bending tests conducted in this study are summarized in Table 2, along with the tempering conditions for the steels and the respective intended use of the results.

3. Microstructural and mechanical test results

3.1 Materials characterization

The initial microstructures of steel B were with minor deviations independent of tempering temperature between 500° and 600°C; steels A500, A550 α and A550 β also exhibited similar microstructures to that of steel B with the exception of the presence of Ti carbide nanoprecipitates. Hence, we will only describe the microstructure of steel B550 as typical for all steels used in this study. The microstructure is modified-ausformed lath martensite with elongated prior austenite grains that consist of parallel arrays or stacks of board- or lath-shaped crystals; an example of this microstructure etched with 3% Nital and picric acid is shown in the optical images presented in Figs. 3a and 3b, respectively. Picric acid etching is effective in revealing the prior austenite grain boundaries clearly. The nominal prior austenite grain-size distribution, as determined using a lineal intercept procedure on optical images, is shown in Fig. 4a. Using ASTM Standard E-112, nominal grain size is 1.128 times as large as the corresponding lineal intercept grain size. The mean nominal prior austenite grain size computed from Fig. 4a to be $56 \pm 25 \mu\text{m}$ with an average aspect ratio of 5.8 ± 3.8 . Deviations 25 μm and 3.8 represent one standard deviation and the same holds for all dimensions reported in this study.

The prior austenite grains are divided into packets, which are groups of parallel laths with the same habit plane. The packet is further divided into several blocks that are defined as parallel lath groups with the same crystal orientation. Orientation imaging microscopy (OIM) was conducted using the SEM-EBSD technique for crystallographic analysis of the microstructure. An inverse pole figure (IPF) map and an image quality map showing grain boundaries with a misorientation angle of $\theta \geq 10.53^\circ$ are presented in Figs. 3c and 3d, respectively. A packet was defined as a group of parallel blocks and the nominal packet size distribution obtained from Figs.

3c and 3d by a lineal intercept procedure is shown in Fig. 4b. The mean nominal packet size was calculated from Fig. 4b as $7.9 \pm 4.7 \mu\text{m}$. Again, the nominal grain size is 1.128 times as large as the corresponding lineal intercept grain size in accordance with the ASTM Standard E-112. A block was defined as a region composed of approximately the same crystal orientation surrounded by high misorientation angle boundaries. Grain boundaries with a misorientation angle $\theta \geq 10.53^\circ$ were defined as high misorientation angle boundaries. In a martensite structure, variants with the Kurdjumov-Sachs (K-S) relationship (Kurdjumov and Sachs, 1930) have a minimum misorientation angle of 10.53° among the six possible block boundaries with the same habit plane (Morito *et al.*, 2003); hence, the lineal intercept length of the high misorientation angle boundaries mainly reflects the size of a block structure. The lineal intercept block width distribution obtained from Figs. 3c and 3d is shown in Fig. 4c, which provides the mean block width $1.2 \pm 0.5 \mu\text{m}$. This block width was slightly smaller than the width determined from high misorientation angle boundaries with $\theta \geq 15.0^\circ$. The lath structure is clearly observed on TEM micrographs; an example is presented in Fig. 3e. The lath width distribution, as measured using a lineal intercept method on the TEM micrographs and shown in Fig. 4d, reveals a mean lath width of $0.38 \pm 0.13 \mu\text{m}$.

The substructure consists of a high density of tangled dislocations (Fig. 3e), cementite particles (Figs. 3e and 3f), inclusions, and nanosized precipitates (Fig. 3g). The dislocation density is quite high to the point that it is difficult to discern one dislocation from another. Needle-shaped and spherical cementite particles are observed at lath boundaries (marked in Figs. 3e and 3f with arrows) as well as within laths (indicated in Figs. 3e and 3f with arrowheads). The cementite particle size distribution, determined from the SEM images, is shown in Fig. 4e; the mean diameter of the cementite particles is $87 \pm 43 \text{ nm}$ and the area fraction is 14.4%. In addition, micrometer-size TiN, AlN, Al_2O_3 and MnS inclusions were confirmed by a combination of SEM and EDX analysis. Nanosized precipitates are dispersed in the matrix as shown in the bright-field electron micrograph presented in Fig. 3g; examples are marked with arrows. The distribution of the nanosized precipitates obtained from the electron micrographs is shown in Fig. 4g; the mean size of these nanosized precipitates is $5.9 \pm 1.7 \text{ nm}$ (Fig. 4f). EDX analysis confirmed these precipitates as carbides containing Ti and Mo, as can be seen by

comparison of the EDX spectra of the matrix and matrix plus a precipitate presented in Figs. 3h and 3i, respectively. Both quantification of the EDX and the extracted residue analysis (Fig. 4g) indicate an atomic ratio Ti:Mo for these nanosized carbide precipitates approximately equal to 1:1. These (Ti,Mo)C precipitates were presumably formed during the hot rolling and tempering; the former type of precipitation is classified as strain-induced precipitation. The coherency of these (Ti,Mo)C precipitates with the matrix was not determined in this study. However, it can be expected that most of the (Ti,Mo)C precipitates in the steel B500 are coherent with the matrix, while they are semi-coherent with the matrix in the B550 and B600 steels, as stated by Wei and Tsuzaki (2006). Not all of nanosized precipitates can be necessarily observed in a transmission electron microscope due to insufficient spatial resolution, weak diffraction contrast caused by small lattice mismatch to the base metal, and so on. The density of the nanosized (Ti,Mo)C precipitates was therefore estimated from a combination of the size obtained by TEM observations and the amount determined by the extracted residue analysis. No retained austenite was detected by TEM observation.

Williamson-Hall plots, $\beta \cos \theta / \gamma$ as a function of $\sin \theta / \lambda$ are presented in Fig. 4h for five strain values in the range of 0.0%–28.3%. Dislocation densities calculated by Eq. (1) are shown plotted in Fig. 4i as a function of strain. The initial dislocation density at a strain 0.0% is $6.7 \times 10^{13} \text{ m}^{-2}$. The dislocation density increases rapidly to $2.3 \times 10^{15} \text{ m}^{-2}$ as the strain is raised to 1.9% and remains almost constant at higher strains up to 28.3%.

The hardness distribution, as determined using a standard 150 kg Rockwell C indent, was uniform across the thickness of each steel plate. This indicates microstructural uniformity of the steel plates through the thickness. For example, hardness R_c for steel B550 was measured as 39.3 and 39.6, respectively at 2.0 and 10.0 mm away from the surface.

3.2 Mechanical test results and the effect of hydrogen

Nominal stress-strain and true stress-strain curves, as determined from a uniaxial tension test of the uncharged steel B550, are presented in Fig. 5. The 0.2% proof stress and ultimate tensile strength are, respectively, 1090 and 1189 MPa with corresponding total elongation and reduction in area of 12.0% and 30.6%. The tensile properties of the uncharged specimens of all 6 steels

investigated are summarized in Table 3. The presence of nanosized (Ti,Mo)C precipitates strengthens steels B by precipitation hardening. This can be confirmed by comparing the yield strengths between steels A500 and B500 and also between steels A550 α and B550 (see Table 3): the yield strengths of steel B are higher than those of steel A irrespective of the longer tempering time. The yield strength of steel A550 β is higher than that of steels A550 α and B550 due to the high heating rate during its tempering process, in other words, due to its shorter tempering time.

GC-TDA spectra from the uncharged and hydrogen-charged steel B550 are presented in Fig. 6a. The exposure conditions of the hydrogen-charged specimens were 31 and 138 MPa hydrogen gas. The uncharged steel does not evolve any hydrogen at temperatures up to 510°C and hence it has no peak 1 hydrogen. The hydrogen-charged steels, on the other hand, show a single broad peak with a prominent desorption rate peak at 190°-194°C. The first peak that appears in a TDA spectrum is defined as peak 1 hydrogen in this study and the hydrogen content in the specimens was determined from this peak. For the hydrogen-charged steel B550 in 31 MPa hydrogen gas, the peak 1 hydrogen that desorbed from room temperature to 435°C is 0.82 mass ppm (45.9 at. ppm). The corresponding peak 1 hydrogen of the steel B550 charged in 138 MPa hydrogen gas was larger by about 2.6 times, *i.e.*, 2.13 mass ppm (118.6 at. ppm).

The impact of hydrogen on the mechanical properties of the steel B550 is shown in the nominal bending stress-displacement curves for the four-point bending tests presented in Fig. 6b. For the uncharged steel B550, the maximum nominal bending stress σ_{nom} is 2128 MPa. In the presence of hydrogen, the nominal stress σ_{nom} at fracture decreases to 1260 and 618 MPa for peak 1 hydrogen contents of 0.82 and 2.13 mass ppm, respectively. The nominal stress gradually decreases with increasing displacement after it reaches the maximum value in all cases, even in the presence of hydrogen. This behavior is different from that exhibited by low-temperature embrittlement where the nominal stress diminishes sharply upon reaching the maximum nominal stress (Nagao *et al.*, 2012a).

The variation of the nominal stress at fracture for the steels A500, A550 β , B500 and B550 with peak 1 hydrogen content is shown in Fig. 6c. The nominal stress at fracture of steels A500 and A550 β declines abruptly as the hydrogen content increases, whereas steels B500 and B550 exhibit a higher resistance to hydrogen embrittlement. Specifically, the nominal stress at fracture

of steel B550 for a hydrogen content of 0.82 mass ppm is 1260 MPa, approximately twice as high as that of steels A500 and A550 β for a hydrogen content of 0.74–0.77 mass ppm (41.0–42.8 at. ppm). The nominal stress at fracture of steel B550 decreases to 618 MPa at the higher hydrogen content of 2.13 mass ppm, the same level as for steels A500 and A550 β .

The hydrogen charging conditions and the resultant peak 1 hydrogen contents, desorption rate peak temperatures, and nominal stresses at fracture of steels A500, A550 β , B500 and B550 are summarized in Table 4. Significantly, a higher hydrogen content was measured in the B500 and B550 steels than in the A500 and A550 β steels at the same hydrogen charging pressure. Also, the desorption rate peak temperature in the TDA spectra of steels B500 and B550 (170°–194°C) was higher than that for steels A500 and A550 β (169°–170°C). The primary microstructural difference between steels A500/A550 β and steels B500/B550 is the presence of nanosized (Ti,Mo)C precipitates in the latter. Accordingly, the higher peak 1 hydrogen content and the higher desorption rate peak temperature of the Ti-added steels should be associated with hydrogen trapping at these precipitates.

The effect of loading displacement rate on the nominal stress at fracture for the B600 steel in the absence and presence of hydrogen is shown in Fig. 7. The uncharged specimens with no peak 1 hydrogen show a slight increase of the fracture stress σ_{nom} with increasing displacement rate. In contrast, the hydrogen-charged specimens in 138 MPa hydrogen gas with 3.12 mass ppm (174.0 at. ppm) peak 1 hydrogen show a rapid increase of the fracture stress with displacement rate. This suggests that hydrogen-induced fracture is diffusion-controlled; more hydrogen becomes available by internal redistribution to the fracture initiation/propagation sites at slower loading rates than at faster loading rates.

SEM images close to the notch root of the interrupted tests with steel A550 α at the onset of fracture are shown in Fig. 8 in the absence and presence of hydrogen. In the absence of hydrogen, fracture initiates directly at the notch root where the local strains are highest, as clearly seen in Figs. 8a and 8b. Figure 8b is a higher magnification image of the boxed region presented in Fig. 8a and a crack is marked with an arrow in Fig. 8b. The nominal stress at fracture in the absence of hydrogen was 2044 MPa. In contrast, fracture initiation in the hydrogen-charged specimen at 138 MPa hydrogen gas with 0.79 mass ppm (44.1 at. ppm) of

peak 1 hydrogen takes place ahead of the notch root, as can be seen from Figs. 8c and 8d, typically close to the elastic-plastic interface where the local tensile stresses are high. Figure 8d is a higher-resolution image of the boxed region shown in Fig. 8c and examples of cracks are indicated with arrows in Fig. 8d. The nominal stress at fracture in the presence of hydrogen was 855 MPa. Although the precise location of crack nucleation is governed by statistical factors, these results clearly reveal that whereas the initial fracture event in the uncharged specimen is locally strain-controlled as the tensile strains are highest at the notch root, the local fracture event for the initiation of hydrogen-induced fracture is a result of a complex interaction between the reduction in fracture strength brought about by the trapped hydrogen, the decohesion caused by the principal normal stress, and the effective shear stress acting on dislocations and piling them up against boundaries, as Novak *et al.* (2010) suggested. Indeed, weakest-link statistics needs to be used to find the probability of fracture initiation in the presence of hydrogen, as discussed in detail in Section 4.

The fracture surface morphologies of steels A500 and B550 are shown and compared in the fractographs in Fig. 9. In the absence of hydrogen, the fracture for both steels predominantly proceeds by ductile microvoid coalescence; a representative microvoid fracture surface from the uncharged steel B550 is shown in Fig. 9c. This was the case for steels A550 α , A550 β , B500 and B600 as well. As for steel A550 α , one uncharged bend specimen was fractured at a displacement rate of 0.1 $\mu\text{m/s}$ and its fracture surface was examined by SEM; the nominal stress at fracture was 2018 MPa.

The fracture surface morphology of hydrogen-charged steel A500 was independent of hydrogen content; it consisted of a mixture of “flat” and “quasi-cleavage” features (Kim and Morris, 1983; Gao and Wei, 1984; Nagao *et al.*, 2012a), with the latter occupying a higher fraction of the surface. Examples of “flat” and “quasi-cleavage” features observed in hydrogen-charged steel A500 in 31 MPa hydrogen gas are presented in Figs. 9a and 9b, respectively. Fine tear ridges (marked with arrows) are frequently observed on the “flat” region (Fig. 9a). The fracture path for this “flat” region is along prior austenite grain boundaries, and as such is categorized as intergranular failure; this is consistent with the results of previous studies using a similar lath martensitic steel (Nagao *et al.*, 2012a, 2014a, 2014b). The “quasi-cleavage” fracture

surface (Fig. 9b) is decorated with fine, lath-like features accompanied by fine serrated markings (indicated with arrows), as well as secondary cracks (shown with arrowheads). The fine, lath-like features are comparable in dimension to the martensite laths (Fig. 3e). The fracture path for this hydrogen-induced “quasi-cleavage” fracture surface is along lath boundaries; this is again consistent with previous studies on a similar lath martensitic steel (Nagao *et al.*, 2012a, 2014a, 2014b). The hydrogen-induced fracture surfaces of steels A550 α and A550 β also showed a mixture of “flat” and “quasi-cleavage” morphologies. As for steel A550 α , one hydrogen-charged bend specimen in 138 MPa hydrogen gas was ruptured at a displacement rate of 0.1 $\mu\text{m/s}$ and its fracture surface was examined by SEM; the nominal stress at fracture was 865 MPa.

In contrast, the fracture surfaces of steel B550 in the presence of hydrogen were dominated by a mixture of “quasi-cleavage” and ductile microvoid coalescence morphologies, irrespective of the hydrogen content; “flat” morphological features were not observed in this hydrogen-charged steel. Representative fractographs of steel B550 with hydrogen contents of 0.82 and 2.13 mass ppm are compared in Figs. 9d, 9e and 9f. With a smaller hydrogen content of 0.82 mass ppm, the hydrogen-induced fracture surface shows a mixed morphology of “quasi-cleavage” and ductile microvoid coalescence (Fig. 9d). The “quasi-cleavage” features become more dominant as the hydrogen content increases to 2.13 mass ppm (Figs. 9e and 9f). Fig. 9f is a higher-resolution SEM image of Fig. 9e. The “quasi-cleavage” morphology appears similar to that seen in the hydrogen-charged A500 steel; fine serrated markings (indicated with arrows) and secondary cracks (shown with arrowheads) are found on fine lath-like features. There is no significant difference found in the morphology of the microvoids between the uncharged (Fig. 9c) and hydrogen-charged (Fig. 9d) specimens of steel B550. It was confirmed by SEM observation that the fracture surfaces of steels B500 and B600 also showed a mixture of “quasi-cleavage” and ductile microvoid features in the presence of hydrogen.

3.3 Hydrogen trap states

Hydrogen traps in steels A and B involve grain boundaries (Li *et al.*, 2004; Novak *et al.*, 2010; Takai and Abe, 2013), dislocations (Sturges and Miodownik, 1969; Oriani, 1970; Hirth, 1980; Choo and Lee, 1982; Birnbaum and Sofronis, 1994; Sofronis and Birnbaum, 1995; Novak

et al., 2010; Itakura *et al.*, 2013), cementite particles (Hong and Lee, 1983a; Hong and Lee, 1983b; Enos and Scully, 2002; Nagao *et al.*, 2012b; Kawakami and Matsumiya, 2013), and inclusions such as TiN, AlN, Al₂O₃ and MnS (Scully *et al.*, 1991; Serra *et al.*, 1997). Specifically, for steel B, nanosized (Ti,Mo)C precipitates (Lee and Lee, 1984; Wei *et al.*, 2004; Wei and Tsuzaki, 2004, 2006; Takahashi *et al.*, 2010; Kawakami and Matsumiya, 2012) are also traps for hydrogen.

In an effort to identify the trapping states and the associated trap binding energies in steels A and B, we analyzed TDA spectra from cathodically-charged steel B (as-quenched and 600°C tempered condition) samples for two different controlled heating rates: 100° and 200 °C /h. The binding energies that we obtained were 57.4, 25.7, 14.0 and 30.5 kJ/mol for high-angle grain boundaries, dislocations, cementite particles, and nanosized (Ti,Mo)C precipitates, respectively. The method of Lee and Lee (1987) was used for dislocations, cementite particles, and nanosized (Ti,Mo)C precipitates; the method of Choo and Lee (1982) and Kissinger (1957) was used for high-angle boundaries. In view of the general scatter in binding energy magnitudes reported in the literature and the complexity of the microstructure of the lath martensitic steels under consideration, we review below the studies of binding energies conducted for ideal microstructures in order to place the above binding energy values into proper perspective.

As previously mentioned, a lath martensitic steel has a four-level hierarchy in its grain-boundary morphology: prior austenite grain, packet, block, and lath boundaries (Morito *et al.*, 2003; Kitahara *et al.*, 2006). Among these four boundaries, prior austenite grain, packet and block boundaries are high-angle grain boundaries, which can hinder the dislocation movement, leading to the formation of dislocation pile-ups at the boundaries (Ueji *et al.*, 2002; Ma *et al.*, 2011). In more detail, a prior austenite grain boundary is a random boundary, whereas each of packet and block boundaries has some variant (orientation) to the prior austenite matrix among 24 possibilities determined by the Kurdjumov-Sachs (K-S) relationship. A lath boundary, on the other hand, is a low-angle grain boundary that is composed of tilt and twist boundaries corresponding to edge and screw dislocations, respectively (Morito *et al.*, 2006). In this work, we took the binding energy of hydrogen to the high-angle prior austenite, packet, and block boundaries equal to 47.4 kJ/mol (Table 5), as determined from the desorption energy reported by

Takai and Abe (2013) in conjunction with the activation energy for hydrogen diffusion, 6.68 kJ/mol (Nelson and Stein, 1973).

The specific hydrogen trap sites at dislocations are elastic fields and cores of edge and screw dislocations (Kumnick and Johnson, 1980; Birnbaum and Sofronis, 1994; Sofronis and Birnbaum, 1995; Itakura *et al.*, 2013). Plastic deformation of body-centered cubic (bcc) steel is governed by screw dislocations rather than edge dislocations due to the smaller mobility of screw dislocations (Saka and Imura, 1972). In addition, hydrogen accumulation in the elastic fields of screw dislocations is considerably smaller as it is governed by the second order modulus interaction (Birnbaum and Sofronis, 1994; Sofronis and Birnbaum, 1995). Thus, in the present study we opted to model the hydrogen/dislocation interactions by considering trapping of hydrogen at screw dislocation cores. Using first-principles calculations, Itakura *et al.* (2013) reported core binding energies equal to 24.7 and 37.6 kJ/mol, respectively for easy and hard core configurations. For our numerical simulations, we took the binding energy of hydrogen to screw dislocation cores equal to 26.0 kJ/mol (Table 5), which is close to the value that we determined by TDA (25.7 kJ/mol).

A lath boundary is composed of edge and screw dislocations. Experimentally measured values of the binding energy to edge and screw dislocations have been reported in the range from 16.7 to 36.4 kJ/mol (Sturges and Miodownik, 1969; Oriani, 1970; Hirth, 1980; Choo and Lee, 1982; Novak *et al.*, 2010). Considering this scatter, a value of 26.0 kJ/mol (Table 5) was assumed for the modeling of trapping of hydrogen at lath boundaries.

Using first-principles calculations, Kawakami and Matsumiya (2013) showed that cementite particles have three specific hydrogen trap states: incoherent and coherent cementite/ferrite interfaces, and octahedral sites in the cementite. The octahedral site cannot be a viable hydrogen trap site at room temperature due to the high activation energy for the introduction of hydrogen into cementite particles, *i.e.*, 59 kJ/mol or higher. Further, there is a large lattice mismatch, larger than 5% (Kawakami and Matsumiya, 2013), between the cementite particles and the matrix, and the measured mean diameter of cementite particles in steel B550 is rather large at 87 nm. Hence, we assumed that the cementite/matrix interface is incoherent with a binding energy for hydrogen equal to 10.9 kJ/mol (Table 5). This value was determined by Hong and Lee (1983b) through a

hydrogen permeation test.

There are no reports in the literature on hydrogen trapping at nanosized (Ti,Mo)C precipitates. However, it is reasonable to assume that the hydrogen trapping state associated with (Ti,Mo)C precipitates is similar to that for nanosized TiC precipitates due to their identical NaCl crystal structure and the Baker-Nutting relationship with respect to the matrix. Takahashi *et al.* (2010) applied a three-dimensional atom probe tomography to directly observe hydrogen trapped at nanosized TiC precipitates. Their results showed that TiC precipitates trap hydrogen on the broad surface of the TiC platelets. Through detailed analysis, they concluded that the carbon vacancies on the surface of the precipitates and the misfit dislocation cores at the interface between TiC precipitates and the matrix are two possibilities for the origin of hydrogen trapping at the interface. The binding energy of hydrogen to coherent or semi-coherent TiC precipitates has been reported to be in the range of 28.1 to 52.3 kJ/mol (Lee and Lee, 1984; Wei *et al.*, 2004; Wei and Tsuzaki, 2006). Referring to the TDA measurements of Lee and Lee (1984), we took the binding energy of hydrogen to nanosized (Ti,Mo)C precipitates to be equal to 28.1 kJ/mol (Table 5), which is very close to the value that we determined by TDA (30.5 kJ/mol).

Lastly, micrometer-size inclusions such as TiN, AlN, Al₂O₃ and MnS that are parts of the microstructures of steels A and B can also act as hydrogen traps. However, it is well established that incoherent TiC precipitates (Wei and Tsuzaki, 2004), incoherent NbC and VC precipitates (Escobar *et al.*, 2013) have a high energy barrier for hydrogen to jump into the incoherent precipitates at room temperature. In fact, in light of the relatively low charging temperature of 250°C that we used, we can further assume that hydrogen is not trapped even at the interface of incoherent precipitates. Thus, we assumed that incoherent micrometer-size inclusions have a negligible effect on hydrogen trapping.

The trap states and the associated binding energies used for the modeling of fracture of steels A and B are summarized in Table 5. We acknowledge here that the magnitudes of the binding energies that we obtained through our own analysis are not identical to those of Table 5. This is mainly due to the difficulties in accurately separating the peaks in the desorption spectra which is associated with the complexity of the microstructure of the lath martensitic steels and also the scattering of the TDA data at the two heating rates. Nevertheless, our calculated binding energies

can be deemed consistent with those reported in the literature.

4. Fracture model

Both “flat” and “quasi-cleavage” fracture surfaces exhibit evidence of ductile processes with fine tear ridges, fine serrated markings and secondary cracks, yet it is unknown if these are an indication that plastic processes are an integral component of hydrogen embrittlement or a consequence of the final separation processes. The latter, even if influenced by hydrogen, may however be irrelevant to determining the rate-limiting process that governs the embrittlement.

To identify and understand the deformation processes that precede fracture as well as the origin of the features on the fracture surface, FIB machining was employed to extract samples from site-specific locations on the hydrogen-induced “flat” and “quasi-cleavage” fracture surfaces of steel A (Nagao *et al.*, 2012a, 2014a, 2014b) and steel B550 (Nagao *et al.*, 2014c). The microstructure immediately beneath the respective fracture surfaces was subsequently examined by TEM.

The bright-field electron micrographs obtained revealed unprecedented microstructural features. Beneath both the hydrogen-induced “flat” and “quasi-cleavage” fracture surfaces, intense slip bands (deformation bands) were observed and lath boundaries were disturbed to the point that they were difficult to discern. Multiple groups of parallel laths were found immediately beneath the “flat” fracture surface, which indicated that the fracture path of the “flat” part was along prior austenite grain boundaries. Thus, we term the “flat” fracture as an intergranular failure. For the “quasi-cleavage” fracture surface, the fracture path was difficult to identify either with block or lath boundaries, and it was accompanied by a step, which corresponded to the fine serrated markings observed on the hydrogen-induced “quasi-cleavage” morphology, as shown in Figs. 9b and 9d-f. As far as the microstructure beneath the fracture surfaces is concerned, for both “flat” and “quasi-cleavage”, the slip bands were inclined with respect to the corresponding surfaces. These findings suggest that hydrogen-induced failure in lath martensitic steels can be attributed to the activation and operation of different slip systems in individual grains, with the enhancement of this dislocation activity by the hydrogen-enhanced localized plasticity (HELP) mechanism (Robertson, 1999; Robertson *et al.*, 2009; Nagao *et al.*,

2015) being of sufficient intensity to disrupt intersected prior austenite (flat surfaces) or block/lath (“quasi-cleavage” surfaces) boundaries. Attendant to this dislocation activity is hydrogen transport and redistribution amongst the lattice and trapping sites that results in enhanced hydrogen accumulation on boundaries (Hwang and Bernstein, 1986; Nagao *et al.*, 1998; Sofronis and Taha, 2000; Dadfarnia *et al.*, 2015), which are further weakened by the locally deposited hydrogen. Intergranular failure appears to occur when slip systems intersect the prior austenite grain boundaries whereas “quasi-cleavage” results when they intersect the lath/block boundaries. Which mode is activated first is dictated by where the local stress accentuation along with the required hydrogen accumulation is attained first. We term this fracture mechanism for the hydrogen embrittlement of the lath martensitic steels under consideration as *hydrogen-enhanced-plasticity-mediated decohesion*.

The above mechanistic discussion is schematically illustrated in Fig. 10. For the hydrogen-induced intergranular fracture, mobile dislocations with their hydrogen atmospheres move within blocks (the basic structural unit surrounded by high-angle grain boundaries in a lath martensitic steel) and are piled up against prior austenite grain boundaries (Model I) or cementite particles on prior austenite grain boundaries (Model II). For the case of hydrogen-induced “quasi-cleavage” failure, mobile dislocations along with their hydrogen atmospheres move within blocks and are piled against cementite particles either on lath boundaries (Model III) or block boundaries (Model V), or cementite precipitates on block boundaries (Model IV). Lath boundaries are low-angle grain boundaries and hence are not favorable sites for dislocations to pile up. However, a dislocation pile-up can form at cementite particles precipitated along lath boundaries, as presented in Figs. 3e and 3f. Packet boundaries are excluded from being possible fracture initiation sites or a propagation path for hydrogen-induced “quasi-cleavage” failure in view of the experimental evidence reported in the preceding paragraph which supports fracture along lath/block boundaries.

Examination of the microstructure immediately beneath the hydrogen-induced intergranular or “quasi-cleavage” transgranular fracture surfaces, yielded no evidence supporting cementite particles being fracture initiation sites or crack propagation paths. Furthermore, both the hydrogen-induced intergranular and “quasi-cleavage” transgranular fractures are often observed

in as-quenched lath martensitic steels that have no cementite precipitation; such an example is provided in Appendix A. Thus, the involvement of cementite particles in the fracture process as outlined in Models II, III and V is less likely. *Therefore, we deem Models I and IV to be the respective mechanistic steps for the generation of the intergranular and “quasi-cleavage” transgranular fractures in the presence of hydrogen.* This mechanism is essentially the same as the one advanced by Novak *et al.* (2010) apart from the difference with regard to the nature of the boundary at which the cracking event takes place. In the Novak model, cracking was considered to initiate by the impingement of a dislocation pile-up on a particle/matrix interface, whereas in the present model, the initiation site is either a prior austenite grain boundary or a block boundary.

We consider quasi-cleavage to be the dominant fracture mechanism also for B type steels, despite the attendant microvoid coalescence morphological features. The reason is that the degree of cleavage-like features on the fracture surface of these steels increased as the hydrogen concentration increased. This result indirectly supports the fact that hydrogen-induced “quasi-cleavage” failure is the dominant controlling mechanism. We argue that microvoid coalescence and local shearing are not the fracture controlling processes but rather a follow up event/process assisted by local stress/strain accentuation in the vicinity of internally nucleated cracks by “quasi-cleavage”. In a recent study, fracture surface topography analysis (FRASTA) was applied to examine the fracture process of a hydrogen-induced lath martensitic steel and it showed that ductile microvoid fracture occurred at the final stage following hydrogen-caused intergranular and “quasi-cleavage” failure (Shibata *et al.*, 2017). This finding also supports that microvoid formation is a follow-up event/process of hydrogen-induced “quasi-cleavage” failure, and the presence of shearing on the ductile-looking part of the fracture surfaces that we observed in the B type steels is unlikely to be the controlling failure process.

We proceed with modeling the intergranular (Model I) and quasi-cleavage (Model IV) fracture events in both steels A and B by adopting the methodology of Novak *et al.* (2010). In particular, we consider both intergranular and quasi-cleavage decohesion taking place along high-angle boundaries and driven by impinging dislocation pile-ups which develop within blocks. The cohesive strength of these boundaries is weakened by the locally trapped hydrogen

and the hydrogen deposited by the impinging dislocations.

Central in the model of Novak *et al.* (2010) is a weakest-link statistical approach to describe the hydrogen-induced fracture events akin to that advanced for cleavage fracture in an AISI 1008 mild steel (Lin *et al.*, 1986). According to weakest-link statistics, the failure probability ϕ of an element with volume dV subjected to a stress σ is given by:

$$d\phi = dV \left(NN_T^{(GB)} \int_0^\sigma g(S) dS \right), \quad (2)$$

where $N_T^{(GB)}$ is the density of the high-angle grain boundaries, N is the fraction of the boundaries that participate in the decohesion process, and the integral denotes the fraction of boundaries with strength less than σ . The volume element, dV , for plane-strain conditions can be considered as $dV = h \times dA$, where dA is the surface area of the element and h is the element thickness taken equal to the average block size. Noting that the total survival probability, $1 - \Phi$, is the product of all the elemental survival probabilities, the total failure probability of the entire specimen is determined through:

$$\Phi = 1 - \exp \left(- NN_T^{(GB)} h \int_A \int_0^\sigma g(S) dS dA \right). \quad (3)$$

The strength of the high-angle grain boundaries, S , can be calculated from the Smith model (1966):

$$\frac{l}{d} S^2 + \tau_{eff}^2 \left[1 + \frac{4}{\pi} \frac{\tau_0}{\tau_{eff}} \sqrt{\frac{l}{d}} \right]^2 = \frac{\pi E \gamma_{eff}}{(1 - \nu^2) d}, \quad (4)$$

where l and d are, respectively, the size of the nucleating crack and the dislocation pile-up length that are assumed to be equal to the block size, h (see distribution in Fig. 4c), γ_{eff} is the effective work of fracture for the grain boundary measured in energy per unit area and a function of hydrogen concentration, E is the Young's modulus, ν is the Poisson's ratio, τ_0 is the friction stress, $\tau_{eff} = \tau_e - \tau_0$ is the effective shear stress, $\tau_e = \sigma_e / \sqrt{3}$ is the applied shear stress, and σ_e is the effective stress. Equation (4) describes a mechanistic fracture model akin to the Griffith model whereby a critical crack forms and propagates unstably when the local energy release rate exceeds the critical value. As such, the model provides an enhanced phenomenological fracture criterion that accounts for the effect of the applied stress as it

develops within the plastic zone ahead of the notch during loading, the local plastic strain that is associated with local dislocation pile-ups, and the reduced critical energy release by the local hydrogen. The hydrogen induced reduction of the critical energy release rate is accounted for through the reduction of γ_{eff} by the hydrogen concentration on the right-hand side, while the effect of the dislocation pile-ups is considered by the second term on the left-hand side of Eq. (4). It should be noted that inherent in the model is the assumption that once formed within the plastic zone and its associated hydrogen environment, the crack propagates unstably. This assumption is in agreement with the experimental observation that cracking zips through block or prior austenite grain boundaries.

Hydrogen solute atoms reside at either normal interstitial lattice sites (NILS) or trapping sites at high-angle grain boundaries (GB), lath boundaries (LB), dislocations (D), cementite particles (C), and nanosized (Ti,Mo)C precipitates (Ti). NILS and trapped hydrogen concentrations are considered to be in equilibrium based on Oriani's equilibrium theory (Oriani, 1970), whereby the occupancy $\theta_T^{(j)}$ of the j^{th} trap type (*i.e.*, GB, LB, D, C, Ti) with a corresponding trap binding energy $W_B^{(j)}$ is related to the NILS occupancy, θ_L , through:

$$\frac{\theta_T^{(j)}}{1-\theta_T^{(j)}} = \frac{\theta_L}{1-\theta_L} \exp\left(\frac{W_B^{(j)}}{RT}\right), \quad K_T^{(j)} = \exp\left(\frac{W_B^{(j)}}{RT}\right), \quad (5)$$

where $K_T^{(j)}$ is the equilibrium constant, R is the universal gas constant, equal to 8.314 J/mol K, and T is the absolute temperature. The hydrogen concentration in NILS, C_L , is given by $C_L = \theta_L \beta N_L$, where β is the number of NILS per solvent atom, $N_L = N_A / V_M$ denotes the density of the solvent atoms, N_A is Avogadro's number, and V_M is the molar volume of the host lattice. The hydrogen concentration in trapping sites is calculated by:

$$C_T^{(j)} = a^{(j)} \theta_T^{(j)} N_T^{(j)}, \quad (6)$$

where $a^{(j)}$ denotes the number of trapping sites per trap of type (j) and $N_T^{(j)}$ is the corresponding trap density. The densities of high-angle grain boundaries, lath boundaries, cementite particles, and nanosized (Ti,Mo)C precipitates are assumed to be constant throughout the deformation. On the other hand, the dislocation trap density varies point-wise as a function of the degree of local effective plastic strain, according to Fig. 4i. The hydrogen transport equation

accounting for stress-driven diffusion through NILS and trapping at all five types of trapping sites is described by Novak *et al.* (2010) and Dadfarnia *et al.* (2011) as:

$$\frac{D}{D_{eff}} \frac{\partial C_L}{\partial t} - DC_{L,ii} + \left(\frac{DV_H}{3RT} C_L \sigma_{kk,i} \right)_{,i} + \left(a^{(D)} \theta_T^{(D)} \frac{\partial N_T^{(D)}}{\partial \varepsilon^p} \right) \frac{d\varepsilon^p}{dt} = 0, \quad (7)$$

where $(\cdot)_{,i} = \partial(\cdot) / \partial x_i$, $\partial / \partial t$ denotes partial derivative with respect to time, V_H is the partial molar volume of hydrogen in solution, σ_{ij} are the Cauchy stress components, ε^p is the effective plastic strain, D is the hydrogen diffusion coefficient through NILS, D_{eff} is an effective diffusion coefficient given by:

$$\frac{D}{D_{eff}} = 1 + \sum_j \frac{\partial C_T^{(j)}}{\partial C_L} = 1 + \sum_j \left(\frac{K_T^{(j)} \alpha^{(j)} N_T^{(j)} / \beta N_L}{[1 + (K_T^{(j)} - 1) C_L / \beta N_L]^2} \right), \quad (8)$$

and the standard summation convention is implied over a repeated index.

The effective work per unit area of grain boundary separation, $2\gamma_{eff}$, is given by:

$$2\gamma_{eff} = 2\gamma_{int} + 2\gamma_p, \quad (9)$$

where $2\gamma_{int}$ is the reversible work of separation and $2\gamma_p$ is the attendant plastic work per unit area (Jokl *et al.*, 1980; Novak *et al.*, 2010). Hydrogen is assumed to reduce the reversible work of decohesion, $2\gamma_{int}$, as described by Hirth and Rice (1980) in terms of the grain-boundary coverage Γ measured in hydrogen atoms per unit area. For the case of fast decohesion (*i.e.*, constant concentration):

$$2\gamma_{int} = (2\gamma_{int})_o - (\Delta g_{GB} - \Delta g_S) \Gamma, \quad (10)$$

where the subscripts *GB* and *S* respectively denote high-angle grain boundaries and free surface created upon separation, $(2\gamma_{int})_o = 2\gamma_S - \gamma_{GB}$ is the reversible work of separation in the absence of hydrogen, γ_S and γ_{GB} are free surface and high-angle grain boundary energies, respectively, in the absence of hydrogen, Δg_{GB} and Δg_S are respectively the Gibbs free energy excesses when hydrogen is absorbed onto the high-angle grain boundary and the free surface created upon separation, which can be calculated through $\Delta g_{GB} = \Delta h_{GB} - T\Delta s_{GB}$, $\Delta g_S = \Delta h_S - T\Delta s_S$; T is the absolute temperature, Δg and Δh are, respectively, the changes of the Gibbs and enthalpy functions upon separation, and Δs is the corresponding entropy change.

According to the thesis of Jokl *et al.* (1980), the plastic work of decohesion γ_p depends on the reversible work γ_{int} and this dependence is characterized by a steep slope. Due to the lack of experimental data, the following form was adopted for this dependence (Novak *et al.*, 2010):

$$\gamma_p = A\gamma_{\text{int}}^m, \quad (11)$$

where A and m are calibration constants.

Decohesion at high-angle grain boundaries is caused by the hydrogen atoms trapped at the grain boundaries, atoms transferred and deposited on the boundaries by moving dislocations, and perhaps by hydrogen in the surrounding NLS. In addition, the deformation and local stresses change the capacity of the boundaries to accommodate hydrogen. Since accurate determination of the hydrogen responsible for the decohesion process is not available, we adopted the following form for the boundary coverage in Eq. (10):

$$\Gamma = \eta \times (10^6 C_T^D / N_L) \times \Gamma_{\text{max}}, \quad (12)$$

where η is a multiplicative factor that can be determined through parametric studies, as will be discussed later. In the above equation, the term C_T^D / N_L denotes the hydrogen concentration at dislocations expressed in H atoms per solvent atom, $\Gamma_{\text{max}} = 4/a^2$ is the maximum coverage assuming 4 tetrahedral sites per unit lattice area on a block boundary, and the parameter η indicates that not all impinging dislocations on high-angle boundaries participate in the decohesion process. The value of η is chosen such that the model predicts the fracture strength for the steel A500 in 31 MPa hydrogen gas, as discussed in Section 5. The underlying principle in the model depicted in Eq. (12) is that the coverage is correlated with the hydrogen deposited on the grain boundary by the dislocations.

5. Modeling results

The zinc-electroplated SE(B) specimens were charged in a hydrogen gas chamber at 250°C for 21 days, a period sufficient for the hydrogen dissolved in the lattice to be in equilibrium with the hydrogen gas at the end of charging time and at a uniform concentration throughout the specimen. This concentration (in at. ppm) is calculated for the quenched and tempered martensitic steels examined in this study using:

$$c_L = 1.345\sqrt{f} \exp(-27200/RT), \quad (13)$$

where the fugacity f is measured in Pa (Nelson and Stein, 1973). According to the Abel-Noble equation of state for hydrogen (*e.g.*, San Marchi *et al.*, 2007), the fugacity is related to the hydrogen gas pressure p by:

$$f = p \exp(pb/RT), \quad (14)$$

where $b = 15.84 \text{ cm}^3/\text{mol}$. From the lattice hydrogen concentration at 250°C and a given hydrogen gas pressure, the hydrogen concentrations in all 5 types of traps were calculated using Eqs. (5) and (6); the calculated trap densities are given in Appendix B. After equilibration, the temperature in the autoclave was reduced to room temperature and the chamber was depressurized. The zinc plating functions as a perfect barrier to hydrogen outgassing during the cooling and depressurization (Nagao *et al.*, 2012b). Thus, assuming that the total hydrogen content at room temperature is the same as in 250°C and, using Eqs. (5) and (6), one can determine the repartitioning of the hydrogen amongst the lattice and trapping sites at room temperature, $T = 25^\circ\text{C}$. This is done by writing the total hydrogen concentration in terms of the lattice occupancy, trap binding energies, trap densities, and temperature, and then by solving the resulting nonlinear equation to find the occupancy at room temperature (see Hosseini *et al.*, 2017 for more rigorous calculation of the hydrogen redistribution between the lattice and traps). Understandably, the individual lattice and trap hydrogen concentrations at room temperature are different for the two types of steels, namely the baseline (steel A) and Ti-added (steel B) steels, because of the presence of the (Ti,Mo)C precipitates in steel B. These lattice and trapped hydrogen concentrations at room temperature were used as initial conditions in our numerical simulations for the hydrogen redistribution in the specimens upon straining; they are reported in Table 6 for the A500, A550 β , B500 and B550 steels at charging pressures between 1 and 138 MPa.

The main difference between steels A and B is the existence of nanosized (Ti,Mo)C precipitates in steel B that act as hydrogen traps. Charging these two types of steels with hydrogen at 250°C and a given pressure yields the same lattice hydrogen concentration and consequently the same concentrations at the trap sites of high-angle grain boundaries, lath boundaries, dislocations, and cementite particles, but steel B can accommodate additional

hydrogen at the (Ti,Mo)C precipitates. Upon hydrogen repartitioning during subsequent cooling and depressurization, (Ti,Mo)C precipitates in steel B trap much of the hydrogen, thus leaving less hydrogen in the lattice, and hence the Ti-added steels (steels B500 and B550) have a smaller lattice hydrogen concentration than the baseline steels (steels A500 and A550 β) at room temperature. The first effect of (Ti,Mo)C precipitates is therefore to reduce the amount of hydrogen dissolved in the lattice and also in other low binding energy sites at lath boundaries, dislocations, and cementite particles at the start of loading. This effect is more pronounced in the B550 steel because the density of (Ti,Mo)C precipitates in this steel is higher than in the B500 steel due to its higher tempering temperature.

Since the specimens are zinc plated and the diffusivity of hydrogen in zinc is several orders of magnitude slower compared to that in martensitic steel, the total hydrogen remains almost unchanged in each steel (A or B) during cooling. By way of example, this constant total concentration along with the individual lattice and trap site concentrations is displayed in the last column of Table 6 under charging at 138 MPa hydrogen gas pressure and 250°C. Upon cooling, hydrogen redistribution takes place while the total hydrogen remains unchanged giving rise to different hydrogen concentrations in lattice and trap sites since the equilibrium constants $K_T^{(j)}$ in Eq. (5) for each trap state are functions of temperature. The equilibrium constants $K_T^{(j)}$ increase as the temperature decreases, which yields a higher occupancy in the traps—it is noted that higher trap binding energy also results in higher trap occupancy. The occupancy of high-angle grain boundaries with binding energy $W_B^{(GB)} = 47.4$ kJ/mol is the highest at room temperature but due to the low density of these traps, the hydrogen concentration trapped at high-angle grain boundaries does not increase substantially. Small changes in trapped concentration are also the case for dislocation traps with $W_B^{(D)} = 26$ kJ/mol because of the low dislocation density before plastic straining. In steels A500 and A550 β , lattice hydrogen moves and gets trapped mainly at lath boundaries at room temperature, but in steels B500 and B550, since the binding energy and density of the (Ti,Mo)C precipitates are higher than those of lath boundaries, most of the lattice hydrogen moves and gets trapped at (Ti,Mo)C precipitates upon cooling. Hydrogen trapped at low binding energy cementites, $W_B^{(C)} = 10.9$ kJ/mol, decreases after cooling from 250° to 25°C although the cementite trap density is the same as the lath trap density. Overall the effect of

(Ti,Mo)C precipitates on hydrogen distribution in steel B is such that whereas steel B has higher total hydrogen concentration than steel A, at room temperature the lattice hydrogen is smaller in steel B.

It is worth noting that the repartitioning of hydrogen between lattice and (Ti,Mo)C precipitate sites is reversed at low hydrogen charging pressures under which a relatively smaller total amount of hydrogen is charged into the steels (*e.g.*, at a pressure of 1 MPa in Table 6). For hydrogen charging pressure of $p < 2.3$ MPa at 250°C, the amount of total hydrogen in steel A is such that after cooling to room temperature, most of the hydrogen is trapped at high-angle grain boundaries with little left to occupy the other traps and lattice sites. However, in steel B, the high-angle grain boundaries cannot accommodate the extra hydrogen released from the (Ti,Mo)C precipitates and therefore the lattice hydrogen concentration in steel B is slightly higher than in steel A, *e.g.*, for the case of charging pressure of 1 MPa shown in Table 6.

The micromechanics of fracture in the SE(B) specimens was modeled by formulating and analyzing the interaction of hydrogen transport with material deformation over the exact SE(B) specimen domain shown in Fig. 2. Due to symmetry, only the right half of the specimen was modeled. The domain was discretized into 10,008 four-noded isoparametric elements with a fine mesh around the notch, as shown in Fig. 11. The initial hydrogen concentrations in the lattice and traps were assumed to be uniform throughout the domain and their magnitude reflected the charging pressure and the type of steel, namely A or B. On the outer boundary of the domain, a zero flux (impermeable) boundary condition was prescribed since the zinc-plating acts as a barrier to hydrogen egress. In the simulations, the specimen was loaded in plane strain at a displacement rate 0.1 $\mu\text{m/s}$, as shown in Fig. 2. On the symmetry line ahead of the notch, a symmetry condition was prescribed: zero shear traction, zero horizontal displacement, and zero flux boundary condition.

The uniaxial tension stress-strain curve obtained experimentally (Fig. 5) was approximated by a power law relationship $\sigma = \sigma_0(1 + \varepsilon^p/\varepsilon_0)^n$, where ε^p is the plastic strain, σ_0 is the initial yield stress, $\varepsilon_0 = \sigma_0/E$, E is Young's modulus, and n is the hardening exponent (which is less than 1). The material properties are given in Table 7. The material was assumed to deform plastically with an associated flow rule based on von Mises yielding. The solution to the

coupled hydrogen diffusion initial/boundary-value problem and the elastoplastic boundary problem was sought numerically through the finite element procedures presented by Sofronis and McMeeking (1989) and Liang and Sofronis (2003).

With $\gamma_s = 1.95 \text{ J/m}^2$ for the surface energy and $\gamma_{GB} = 0.78 \text{ J/m}^2$ for the grain boundary energy (Hirth and Lothe, 1992), the reversible work of decohesion in the absence of hydrogen is $(2\gamma_{\text{int}})_0 = 2\gamma_s - \gamma_{GB} = 3.12 \text{ J/m}^2$. Assuming $\gamma_{\text{eff}} = 23 \text{ J/m}^2$ in the absence of hydrogen (Lin *et al.*, 1986; Novak *et al.*, 2010) and using Eq. (9), Eq. (11) was calibrated with $m = 6$ and $A = 1.488$. For the segregation enthalpies of hydrogen to the high-angle grain boundaries and to the free surface, it was considered that $\Delta h_{GB} = -W_B^{(GB)} = -47.4 \text{ kJ/mol}$ and $\Delta h_s = -95.5 \text{ kJ/mol}$ (Hirth, 1980), respectively. For the segregation entropy terms, it was assumed that $\Delta s_{GB} = 25 \text{ J/mol}$ and $\Delta s_s = 15 \text{ J/mol}$ (Rice and Wang, 1989).

For the friction stress in Eq. (4), it was assumed that $\tau_0 = 0.001\mu$, where $\mu = 76.9 \text{ GPa}$ is the shear modulus. In Eq. (3), it was considered that $N = 0.2\%$ for the fraction of the high-angle grain boundaries that participate in the decohesion process and $N_T^{(GB)} = 1.24 \times 10^{16}$ for the number density of the high-angle grain boundaries per unit volume. The total failure probability of the entire specimen was calculated by Eq. (3). At each increment of the applied boundary displacement, the principal normal stress, σ , at each integration point was obtained and the fraction of the boundaries with strength less than σ was calculated using Eq. (4) and the distributions of the nucleated crack size l and dislocation pile-up length d . Both l and d were assumed to be the block size h shown in Fig. 4c. The failure load (applied displacement) was defined as the displacement at which the total failure probability was $\Phi = 50\%$.

The maximum nominal stress, *i.e.*, the nominal stress at fracture, for steel A500 charged in hydrogen gas, was used to calibrate the fracture model. To predict the nominal stress at fracture $\sigma_{\text{nom}} = 575 \text{ MPa}$ for this steel A500 charged in 31 MPa hydrogen gas, the value of 0.2 was adopted for the multiplicative factor, η , in Eq. (12). Furthermore, it was assumed that hydrogen does not reduce the reversible work of separation below $(2\gamma_{\text{int}}) = 2.09 \text{ J/m}^2$ (*i.e.*, $\gamma_{\text{int}} \geq 1.045 \text{ J/m}^2$) which corresponds to a minimum effective work of separation of $2\gamma_{\text{eff}} = 6.0 \text{ J/m}^2$ (*i.e.*, $\gamma_{\text{eff}} \geq 3.0 \text{ J/m}^2$). Note that a 33% reduction in γ_{int} (from 1.56 J/m^2 in the absence of hydrogen to 1.045 J/m^2 in the presence of hydrogen) yields an 87% reduction in

γ_{eff} (from 23 J/m² in the absence of hydrogen to 3.0 J/m² in the presence of hydrogen) due to the strong dependence of the plastic fracture energy, γ_p , on γ_{int} , see Eq. (11). Adopting such a maximum reduction of the reversible work of separation by hydrogen yielded a nominal stress at fracture equal to 606 MPa, close to the failure stress measured experimentally. It is interesting that Wang *et al.* (2016) using atomistic simulations calculated that the hydrogen induced reduction of the grain boundary cohesive energy in iron cannot be greater than ~30%—a reduction that can only take place at hydrogen pressures on the order of GPa, *i.e.*, at pressures far above than those prevalent in experimental investigations of hydrogen embrittlement. Similarly, Martinez-Paneda *et al.* (2016) assumed approximately a 50% cohesion reduction to fit experimental data for a high strength austenitic Ni-Cu superalloy (Monel K-500) using strain gradient plasticity for the constitutive response of the material. In summary, a ~33% maximum cohesive energy reduction is not an unrealistic assumption in order to fit our experimental data.

Figure 12 shows contour plots of the numerical simulation results for steels A500 (Figs. 12a, 12c, 12e, and 12g) and B550 (Figs. 12b, 12d, 12f, and 12h) at the moment of specimen failure. Both steels were charged at 31 MPa and the initial hydrogen concentrations in NISL throughout the specimens prior to loading were 1.054 and 0.1673 at. ppm for the A500 and B550 steels, respectively. The maximum principal stress, σ_I (Figs. 12a and 12b), the effective stress that is responsible for the dislocation pile-up formation, σ_e (Figs. 12c and 12d), the normalized hydrogen concentration trapped at dislocations, $C_T^{(D)} / N_L$ (Figs. 12e and 12f), and the fraction of debonded high-angle grain boundaries, $\int g(S) dS$, (Figs. 12g and 12h) are compared. As expected, the hydrogen concentration at dislocation traps has a marked effect on failure and this becomes evident by comparing the fraction of debonded boundaries (Figs. 12g and 12h) with the hydrogen concentration profiles (Figs. 12e and 12f). We note though that the failure of the boundaries is a result of the interaction between fracture strength reduction by hydrogen and boundary separation by the principal normal stress.

The model predictions for the normalized nominal stress σ_{nom} / σ_0 at which the A500, A550 β , B500 and B550 steels failed as a function of the hydrogen charging pressure are shown in Fig. 13. The data for the A500 and A550 β steels are combined in Fig. 13a, with Figs. 13b and

13c, respectively presenting the model predictions for the B500 and B550 steels. Superposed on these figures are the experimental data for the nominal stress at fracture for uncharged and hydrogen-charged specimens at 31 or 138 MPa hydrogen gas. The agreement between the model predictions and the experimental measurements is rather satisfactory. Steels A500 and A550 β show steep reduction in fracture strength as the charging pressure increases. The presence of (Ti,Mo)C in steels B500 and B550 alleviates such a decrease by removing hydrogen from the lattice, which in turn results in less hydrogen trapped at dislocations.

6. Discussion

We have attempted here to present quantitative predictions of the onset of hydrogen-induced intergranular and “quasi-cleavage” transgranular fractures commonly observed in lath martensitic steels by using the statistical, physical-based, micro-mechanical approach of Novak *et al.* (2010). Based on the experimental evidence, we modeled the failure event in terms of decohesion at high-angle boundaries which are the sites of the experimentally observed decohesion at prior austenite grain (intergranular failure) or block boundaries (“quasi-cleavage” transgranular failure). Decohesion is driven by dislocation pile ups which have been experimentally observed to impinge on the failed high-angle boundaries at an angle and is assisted by the weakening of these boundaries by hydrogen. The binding energy of the high-angle boundaries is 47 kJ/mol and as a result they remain fully saturated with hydrogen throughout loading to failure. Hence, as in the model of Novak *et al.* (2010), hydrogen deposited on the grain boundaries by dislocations is essential to the cohesion weakening. It should be noted that the hydrogen populations at NILS and low binding energy traps, such as lath boundaries, dislocations, and cementite particles, vary with straining. This fracture model is a demonstration of a concerted action of the HELP mechanism that brings about the required stress through slip banding against the high-angle boundaries and the HEDE mechanism whose operation is assisted by the hydrogen deposited on the boundaries through the HELP mechanism. We term this coupled HELP- plus HEDE-induced failure process as *hydrogen-enhanced-plasticity mediated decohesion*. We emphasize again that recent experimental observations of the microstructure beneath hydrogen-induced intergranular and “quasi-cleavage” transgranular fracture surfaces

using TEM studies of FIB lift-out samples inform this mechanistic framework.

The weakest-link statistical approach was applied by assuming the size of dislocation pile-up and the length of the incipient microcrack were set by the block size, as blocks represent the smallest basic structural unit with high-angle grain boundaries in a lath martensitic steel. Thus, for the estimation of the statistical distribution of strengths of the high-angle boundaries, the distribution shown in Fig. 3c for the block size was used. For the treatment of the effect of hydrogen solutes on the reversible work of separation, as shown by Eq. (12), we considered that hydrogen deposited by dislocations, $C_T^{(D)}$, contributes to the weakening of the grain boundaries. Novak *et al.* (2010) in their corresponding Eq. (10) considered only the occupancy of the hydrogen trapped at dislocations, $\theta_T^{(D)}$. Definitely, this apparent difference between the two treatments could be removed by considering in Eq. (12) only the contribution of $C_T^{(D)}$, and to weight it with a larger multiplicative factor η . The issue of the type of hydrogen responsible for the decohesion event, as discussed by Novak *et al.* (2010), is intimately related to the local micromechanics of the microcrack nucleation. More specifically, the hydrogen responsible for the debonding of the interface may comprise the hydrogen trapped at the grain boundary, the hydrogen deposited by the impinging dislocations and the hydrogen in the surrounding normal interstitial sites. In this work, the fact that the use of a multiplicative factor $\eta = 100$ yields model predictions close to the experimental data implies that all three types of hydrogen, namely lattice hydrogen and hydrogen trapped at high-angle grain boundaries and dislocations, are involved in the decohesion event. This issue requires further investigation.

For a closed system, the presence of nanosized (Ti,Mo)C precipitates decreases the amounts of hydrogen in the lattice and at the dislocations, provided that the precipitates are not saturated prior to loading. As a result, the high-angle boundaries in the Ti-added steels are weakened less and this explains the macroscopically observed higher resistance of these steels to hydrogen embrittlement. However, if the initial hydrogen concentration is large enough for the (Ti,Mo)C precipitates to be saturated before loading, then the mitigating effect of these precipitates is lost. So the potential for mitigation depends on the initial hydrogen concentration in the closed system and, of course, on the density of (Ti,Mo)C precipitates. Lath martensitic steels can be designed to contain various kinds of nanosized precipitates, such as TiC, V_4C_3 , and NbC. If the binding

energy for hydrogen trapping at such nanosized precipitates is high enough and the density is such that they are fully saturated with hydrogen prior to loading, the mitigating effect on hydrogen embrittlement, as observed in the present study, would not be realized. For instance, a design with VC precipitates with a binding energy 26.3-28.3 kJ/mol (Asahi *et al.*, 2003) can be hydrogen resistant, whereas a corresponding design based on coherent TiC precipitates with a binding energy greater than 45 kJ/mol (Wei *et al.*, 2004; Wei and Tsuzaki, 2006) or incoherent TiC precipitates with a binding energy between 79.0 and 109.3 kJ/mol (Wei *et al.*, 2004) would be less likely to be resistant. In fact, the beneficial effect of nanosized vanadium carbides on hydrogen tolerance has already been observed in the experimental investigations of Asahi *et al.* (2003) and Lee *et al.* (2016). Lastly, precipitates with very low binding energy would also not be effective in reducing the susceptibility to hydrogen embrittlement as they cannot effectively deplete the hydrogen concentrations in the lattice and at dislocations.

7. Conclusions

The statistical, physical-based, micro-mechanical model of Novak *et al.* (2010) has been applied to quantitatively predict the hydrogen-induced intergranular and “quasi-cleavage” transgranular fractures commonly observed in lath martensitic steels. The basic fracture mechanism that we propose, termed *hydrogen-enhanced-plasticity mediated decohesion*, involves debonding of high-angle grain boundaries by impinging dislocation pile-ups. The debonding is facilitated by the weakening of the boundaries from hydrogen residing in the grain boundaries and the lattice, and the hydrogen deposited on the boundaries by impinging dislocations. In this regard, the introduction of nanosized (Ti,Mo)C precipitates improves the resistance to hydrogen embrittlement, as the presence of such precipitates acts to diminish the amounts of hydrogen redistributed to the grain boundaries by lattice diffusion and dislocations. It is important to note that the essential characteristics of these precipitates for mitigating hydrogen embrittlement are their *moderate* binding energy and density. Precipitates with high or low binding energy and relatively low density are less likely to have such a mitigation effect.

Acknowledgements

The authors gratefully acknowledge funding from the JFE Steel Corporation and the support of the International Institute for Carbon Neutral Energy Research (WPI-I2CNER), sponsored by the World Premier International Research Center Initiative (WPI), MEXT, Japan. The involvement of ROR was additionally supported by the Mechanical Behavior of Materials Program (KC13) at the Lawrence Berkeley National Laboratory (LBNL) funded by Office of Science, Office of Basic Energy Sciences, Materials Sciences Division of the U.S. Department of Energy under contract no. DE-AC02-05CH11231. The authors would also like to acknowledge Prof. I. M. Robertson and Dr. S. Wang at the University of Wisconsin-Madison for fruitful discussions. A.N. acknowledges and thanks the laboratory members of the I.M.R. group, especially K.E. Nygren and M.L. Martin for assistance, support and discussions. The microscopy work was carried out in part at the Center for Microanalysis of Materials in the Frederick Seitz Materials Research Laboratory at the University of Illinois at Urbana-Champaign. Exposure of the Zn-plated steel specimens to high-pressure hydrogen gas was performed by J. A. Campbell in the Hydrogen Effects on Materials Laboratory at Sandia National Laboratories (Livermore, CA, USA).

Appendix A. An example of intergranular and “quasi-cleavage” transgranular fracture of an as-quenched lath martensitic steel with no cementite particle precipitation

A steel plate with a thickness of 25 mm that contained chemical compositions of 0.29C-0.31Si-1.07Mn-0.008P-0.0035S-0.026Al soluble-0.0038Total N-others (mass%) was reheated to transform into austenite and then quenched in water to obtain an as-quenched lath martensitic steel structure. Subsequently, a uniaxial tension test was performed at room temperature in the presence of hydrogen. The SEM image of the microstructure, which was etched with 3% Nital, is presented in Fig. 14a. No cementite particles were observed on the lath martensite structure. The hydrogen-induced fracture surface shows a mixed morphology of “flat” intergranular (Fig. 14b) and “quasi-cleavage” (Fig. 14c). These fracture surface morphologies therefore appear irrespective of the existence of cementite particles.

Appendix B. Determination of the hydrogen trap densities

As discussed in Section 3.3, the hydrogen trap sites in the A500, A550 β , B500 and B550 steels are commonly high-angle grain boundaries (prior austenite grain, packet and block boundaries), low-angle grain boundaries (lath boundaries), dislocations and cementite particles. Steels B500 and B550 have nanosized (Ti,Mo)C precipitates that act as an additional trap site. For the binding energy of each trap type, the values provided in Table 5 were used: $W_B^{(GB)} = 47.4$ kJ/mol for high-angle grain boundaries, $W_B^{(LB)} = 26.0$ kJ/mol for lath boundaries, $W_B^{(D)} = 26.0$ kJ/mol for dislocations, $W_B^{(C)} = 10.9$ kJ/mol for cementite particles, and $W_B^{(Ti)} = 28.1$ kJ/mol for (Ti,Mo)C precipitates.

The dislocation trap density as a function of plastic strain was determined through XRD measurements. Note that this density consists of all the dislocations, including those on the lath boundaries. Assuming one trap per atomic plane threaded by a dislocation line (Tien *et al.*, 1976; McLellan, 1979), one can express the dislocation trap density as $N_T^{(D)} = \sqrt{2}\rho/a$, where the lattice parameter $a = 0.2867$ nm. Thus, the dislocation trap density can be assessed as $N_T^{(D)} = 3.31 \times 10^{23}$ traps/m³ prior to deformation, it increases linearly with plastic strain up to 1.13×10^{25} traps/m³ at 1.9% plastic strain, and remains constant with further plastic straining. We can also assume that there is one trapping site per dislocation trap, *i.e.*, $\alpha^{(D)} = 1$. Here we would like to draw attention to the fact that the assumed dislocation trap density model does have an effect on the model's fracture predictions. This is because we assumed that the hydrogen coverage of the debonding boundary, as calculated by Eq. (12), does depend on the dislocation trap model through the corresponding dislocation trap concentration. However, since the multiplicative factor η in Eq. (12) is chosen such that the model predictions match the experimental results for the steel A500 charged in 31 MPa hydrogen gas (see Section 5), a different dislocation trap model would require a different multiplicative factor η . Certainly this dependence of the fitting parameter η on the dislocation trap model is worth investigating and this can be the subject of a subsequent work. Novak *et al.* (2010) investigated such a dependence in their Appendix C.3 and concluded that their predictions for the Sofronis *et al.* (2001) model for trapping at dislocations and for the Kumick and Johnson model (1980) are insensitive to the

model used. The reason for this dislocation density insensitivity of the Novak *et al.* model derives from the fact that the hydrogen coverage for the debonding interface, as calculated by their Eq. (10), is a function of the dislocation trap occupancy and not of the dislocation density, *i.e.*, of the dislocation trap model. In the present study, we used our own experimental measurements of the dislocation density for the material that we investigated, *i.e.*, steel B550, to determine the density of traps associated with dislocations. Incidentally, the dislocation trap densities of the present study are close to those assumed in the work of Sofronis *et al.* (2001).

First, the microstructural characteristics of the lath boundaries and cementite particles (Figs. 4d and 4e) were used to calculate approximate values for the trap densities at cementite particles and lath boundaries. The area fraction of cementite particles (of 14.4%) and the distribution of the cementite particle sizes give an estimated average distance between the cementite particles, $L^{(C)} \approx 0.236 \mu\text{m}$, from which the volume density of the cementite particles can be calculated as $N_T^{(C)} \approx (1/L^{(C)})^3 \approx 7.6 \times 10^{19} \text{ particles/m}^3$. The number of H trap sites per cementite particle can be estimated by $\alpha^{(C)} \approx (\sum \pi (d_i^{(C)})^2 f_i^{(C)}) \times 4/a^2 \approx 1.6 \times 10^6 \text{ sites/particle}$, where a is the lattice parameter, $d_i^{(C)}$ and $f_i^{(C)}$ are, respectively, the cementite particle size and the associated frequency, as given in Fig. 4e. Assuming naturally that there are 4 tetrahedral sites per unit lattice area that can be occupied by hydrogen, we obtain an approximation for the cementite trap site density as $\alpha^{(C)} N_T^{(C)} \approx 1.19 \times 10^{26} \text{ sites/m}^3$. For the lath boundaries, given that the lath width $h^{(Lath)}$ is much smaller than the other lath dimensions, the lath boundary area density can be estimated as $1/h^{(Lath)}$ and thus $\alpha^{(LB)} N_T^{(LB)} \approx 4/a^2 h^{(Lath)} \approx 1.28 \times 10^{26} \text{ sites/m}^3$. These estimations indicate that the hydrogen trap densities at cementite particles and lath boundaries are about the same.

Next, to determine the trap densities of high-angle grain boundaries, lath boundaries and cementite particles in the A500, A550 β , B500 and B550 steels, and also the trap site density of (Ti,Mo)C precipitates in Ti-added B500 and B550 steels, the hydrogen content in the two steel systems, measured by TDA, was utilized. The experimentally measured hydrogen content for the A500 and A550 β steels charged at hydrogen gas pressure of 31 MPa was 28.4 and 24.6 at. ppm, respectively. Charging the steels at 138 MPa hydrogen gas, this hydrogen content increased respectively to 42.8 and 41.0 at. ppm. Since steel A does not contain any Ti, the experimental

results for this steel can be used to determine the trap site densities of the high-angle grain boundaries, $\alpha^{(GB)}N_T^{(GB)}$, lath boundaries, $\alpha^{(LB)}N_T^{(LB)}$, and cementite particles, $\alpha^{(C)}N_T^{(C)}$. After obtaining these trap site densities, the trap site density of the (Ti,Mo)C precipitates, $\alpha^{(Ti)}N_T^{(Ti)}$, is calculated using the experimentally measured hydrogen content in the Ti-added steel B. This hydrogen content was 39.5 and 88.6 at. ppm for steel B500 and 45.9 and 118.6 at. ppm for steel B550 charged at hydrogen pressures of 31 and 138 MPa, respectively. It should be noted that lath boundaries trap hydrogen at the interface itself as well as at dislocations that compose the boundaries.

The calculation of the $\alpha^{(i)}N_T^{(i)}$ values was carried out as follows: it was assumed that hydrogen at trap sites is in equilibrium with the lattice hydrogen as per the Oriani's theory (Eq. (5)). The lattice hydrogen concentration was obtained from Eq. (13). The total hydrogen concentration equals the sum of the hydrogen concentrations in the lattice and traps. As the specimens had a zinc-plating deposited on their surfaces as a barrier to hydrogen egress, the total hydrogen content in the specimens did not change after the specimens reached equilibrium with hydrogen gas at 250°C. Thus, guided by the estimated values of $\alpha^{(C)}N_T^{(C)}$ and $\alpha^{(LB)}N_T^{(LB)}$, we carried out a parametric study of the trap densities of high-angle grain boundaries, lath boundaries, and cementite particles. Based on this study, the values $\alpha^{(GB)}N_T^{(GB)} = 5.0 \times 10^{23}$ sites/m³ and $\alpha^{(C)}N_T^{(C)} = \alpha^{(LB)}N_T^{(LB)} = 3.0 \times 10^{25}$ sites/m³ yielded a calculated hydrogen content for the A500 and A550 β steels close to the hydrogen content obtained by TDA. These calculated values are 20.1 and 48.6 at. ppm, respectively, for charging at 31 and 138 MPa hydrogen gas at 250°C for the A500 and A550 β steels.

Given that the trap characteristics of all the A and B steels are the same, except for the nanosized (Ti,Mo)C precipitates in the Ti-added ones, the best values for the (Ti,Mo)C trap density in steels B500 and B550 were determined to be $\alpha^{(Ti)}N_T^{(Ti)} = 1.45 \times 10^{26}$ and 2.4×10^{26} sites/m³, respectively. Using these trap densities, the total hydrogen contents in steel B500 charged in 31 and 138 MPa hydrogen gas at 250°C were calculated as 36.6 and 90.4 at. ppm, respectively. For the B550 steel charged in 31 and 138 MPa hydrogen gas pressure, the calculated total hydrogen concentrations were 47.5 and 117.8 at. ppm, respectively. These calculated hydrogen concentrations are all close to those measured experimentally.

Erratum to: “A statistical, physical-based, micro-mechanical model of hydrogen-induced intergranular fracture in steel,” P. Novak, R. Yuan, B. P. Somerday, P. Sofronis and R. O. Ritchie, *J. Mech. Phys. Solids* 58 (2010) 206-226.

1) The right-hand side of Eq. (4) in the referenced paper should be corrected to represent penny-shaped crack as follows:

$$\frac{l}{d} S^2 + \tau_{eff}^2 \left[1 + \frac{4}{\pi} \frac{\tau_0}{\tau_{eff}} \sqrt{\frac{l}{d}} \right]^2 = \frac{\pi E \gamma_{eff}}{(1-\nu^2)d}.$$

Note that $\tau_{eff} = \tau_e - \tau_0$ where $\tau_e = \sigma_e / \sqrt{3}$ and $\sigma_e = \sqrt{3/2 \sigma'_{ij} \sigma'_{ij}}$ is the effective stress. If $\tau_e < \tau_0$ then the second term on the left side of the above equation (Eq. (4) in the referenced paper) is set to zero.

2) The multiplicative factor η in Eq. (10) of the referenced paper is $\eta = 0.002$.

3) A typographic error for the value and units of the lattice site density N_L in their Table 3 should be corrected to 8.64×10^{28} (atoms/m³).

These corrections are inconsequential to all the predictions in the paper, which are deemed to remain accurate.

References

- Andrews, K.W., 1965. Empirical formulae for the calculation of some transformation temperatures. *J. Iron Steel Inst.* 203, 721-727.
- Asahi, H., Hirakami, D., Yamasaki, S., 2003. Hydrogen trapping behavior in vanadium-added steel. *ISIJ Int.* 43, 527-533.
- Bandyopadhyay, N., Kameda, J., McMahon Jr., C.J., 1983. Hydrogen-induced cracking in 4340-type steel: effects of composition, yield strength and H₂ pressure. *Metall. Trans. A* 14A, 881-888.

- Beachem C.D., 1972. A new model for hydrogen-assisted cracking (hydrogen “embrittlement”). *Metall. Trans. B* 3, 437-451.
- Birnbaum, H.K., Sofronis, P., 1994. Hydrogen-enhanced localized plasticity—a mechanism for hydrogen-related fracture. *Mater. Sci. Eng. A* 176, 191-202.
- Birnbaum, H.K., Robertson, I.M., Sofronis, P., and Teter, D. 1997. Mechanisms of hydrogen related fracture—a review. In: Magnin, T. (Ed.), *Corrosion Deformation Interactions CDI’96* (2nd Intl. Conf., Nice, France, 1996). The Institute of Materials, UK, pp. 172–195.
- Choo, W.Y., Lee, J.Y., 1982. Thermal analysis of trapped hydrogen in pure iron. *Metall. Trans. A* 13A, 135-140.
- Dadfarnia, M., Martin, M.L., Nagao, A., Sofronis, P., Robertson, I.M., 2015. Modeling hydrogen transport by dislocations. *J. Mech. Phys. Solids* 78, 511-525.
- Dadfarnia, M., Sofronis, P., Neeraj, T., 2011. Hydrogen interaction with multiple traps: can it be used to mitigate embrittlement? *Int. J. Hydrogen Energy* 36, 10141-10148.
- Enos, D.G., Scully, J.R., 2002. A critical-strain criterion for hydrogen embrittlement of cold-drawn, ultrafine pearlitic steel. *Metall. Mater. Trans. A* 33A, 1151-1166.
- Escobar, D.P., Duprez, L., Atrens, A., Verbeken, K., 2013. Thermal desorption spectroscopy study of experimental Ti/S containing steels. *Mater. Sci. Tech.* 29, 261-267.
- Gangloff, R.P., Somerday, B.P. (Eds.), 2012. *Gaseous hydrogen embrittlement of materials in energy technologies*. Woodhead Publishing, Cambridge.
- Gao, M., Wei, R.P., 1984. Quasi-cleavage and martensite habit plane. *Acta Metall.* 32, 2115-2124.
- Gerberich, W.W., Livne, T., Chen, X.-F., Kaczorowski, M., 1988. Crack growth from internal hydrogen—temperature and microstructural effects in 4340 steel. *Metall. Trans. A* 19A, 1319-1334.
- Gerberich WW, Marsh PG, Hoehn JW (1996) Hydrogen induced cracking mechanisms - are there critical experiments? In: Thompson AW, Moody NR (eds) *Hydrogen effects in materials*, TMS, Warrendale, PA, pp 539-551.

- Hirth, J.P., 1980. Effects of hydrogen on the properties of iron and steel. *Metall. Trans. A* 11A, 861-890.
- Hirth, J.P., Lothe, J., 1982. *Theory of Dislocations*, second edition. John Wiley & Sons, New York, NY.
- Hirth, J.P., Rice, J.R., 1980. On the thermodynamics of adsorption at interfaces as it influences decohesion. *Metall. Trans. A* 11A, 1501-1511.
- Hong, G.-W., Lee, J.-Y., 1983a. The measurement of the trap binding energy by the thermal analysis technique. *Scr. Metall.* 17, 823-826.
- Hong, G.-W., Lee, J.-Y., 1983b. The interaction of hydrogen and the cementite–ferrite interface in carbon steel. *J. Mater. Sci.* 18, 271-277.
- Hosseini, Z.S., Dadfarnia, M., Nibur, K.A., Somerday, B.P., Gangloff, R.P., and Sofronis, P., 2017. Trapping against hydrogen embrittlement. In: Somerday, B.P., Sofronis, P. (eds.) 2016 International hydrogen conference: Materials performance in hydrogen environments, ASME Press, New York, NY, pp. 71-80.
- Hwang, C., Bernstein, I.M., 1986. Dislocation transport of hydrogen in iron single crystals. *Acta Metall.* 34, 1001-1010.
- Itakura, M., Kaburaki, H., Yamaguchi, M., Okita, T., 2013. The effect of hydrogen atoms on the screw dislocation mobility in bcc iron: a first-principles study. *Acta Mater.* 61, 6857-6867.
- Jokl, M.L., Vitek, V., McMahon Jr., C.J., 1980. A microscopic theory of brittle fracture in deformable solids: a relation between ideal work to fracture and plastic work. *Acta Metall.* 28, 1479-1488.
- Kawakami, K., Matsumiya, T., 2012. Numerical analysis of hydrogen trap state by TiC and V_4C_3 in bcc-Fe. *ISIJ Int.* 52, 1693-1697.
- Kawakami, K., Matsumiya, T., 2013. *Ab-initio* investigation of hydrogen trap state by cementite in bcc-Fe. *ISIJ Int.* 53, 709-713.
- Kim, Y.H., Morris Jr., J.W., 1983. The nature of quasicleavage fracture in tempered 5.5Ni steel after hydrogen charging. *Metall. Trans. A* 14A, 1883-1888.
- Kissinger, H. E., 1957. Reaction Kinetics in Differential Thermal Analysis. *Anal. Chem.*, 29,

1702–1706.

- Kitahara, H., Ueji, R., Tsuji, N., Minamino, Y., 2006. Crystallographic features of lath martensite in low-carbon steel. *Acta Mater.* 54, 1279-1288.
- Krauss, G., 1990. *Steels: heat treatment and processing principles*. ASM International, Materials Park, OH.
- Kumnick, A.J., Johnson, H.H., 1980. Deep trapping states for hydrogen in deformed iron. *Acta Metall.* 28, 33-39.
- Kurdjumov, G.V., Sachs, G., 1930. Over the mechanisms of steel hardening. *Z. Phys.* 64, 325-343.
- Lee, J., Lee, T., Kwon, Y.J., Mun, D.-J., Yoo, J.-Y., Lee, C.S., 2016. Effect of vanadium carbides on hydrogen embrittlement of tempered martensitic steel. *Met. Mater. Int.* 22, 364-372.
- Lee, J.Y., Lee, J.L., 1987. A Trapping theory of hydrogen in pure iron. *Phil. Mag. A*, 56, 293-309.
- Lee, H.G., Lee, J.-Y., 1984. Hydrogen trapping by TiC particles in iron. *Acta Metall.* 32, 131-136.
- Li, D., Gangloff, R.P., Scully, J.R., 2004. Hydrogen trap states in ultrahigh-strength AERMET 100 steel. *Metall. Mater. Trans. A* 35A, 849-864.
- Liang, Y., Sofronis, P., 2003. Micromechanics and numerical modelling of the hydrogen-particle-matrix interactions in nickel-base alloys. *Model. Simul. Mater. Sci. Eng.* 11, 523-551.
- Lin, T., Evans, A.G., Ritchie, R.O., 1986. A statistical model of brittle fracture by transgranular cleavage. *J. Mech. Phys. Solids* 34, 477-497.
- Lynch, S.P., 1984. A fractographic study of gaseous hydrogen embrittlement and liquid-metal embrittlement in a tempered-martensitic steel. *Acta Metall.* 32, 79-90.
- Ma, X.P., Wang, L.J., Liu, C.M., Subramanian, S.V., 2011. Role of Nb in low interstitial 13Cr super martensitic stainless steel. *Mater. Sci. Eng. A* 528, 6812-6818.
- Martinez-Paneda, E., Niordson, C.F., Gangloff, R.P., 2016, Strain gradient plasticity-based modeling of hydrogen environment assisted cracking. *Acta Mater.* 117, 321-332.

- McLellan, R.B., 1979. Thermodynamics and diffusion behavior of interstitial solute atoms in non-perfect solvent crystals. *Acta Metall.* 27, 1655-1663.
- Morito, S., Huang, X., Furuhashi, T., Maki, T., Hansen, N., 2006. The morphology and crystallography of lath martensite in alloy steels. *Acta Mater.* 54, 5323-5331.
- Morito, S., Tanaka, H., Konishi, R., Furuhashi, T., Maki, T., 2003. The morphology and crystallography of lath martensite in Fe-C alloys. *Acta Mater.* 51, 1789-1799.
- Nagao, A., Dadfarnia, M., Sofronis, P., Robertson, I.M., 2015. Hydrogen embrittlement mechanisms. In: Totten, G.E., Colás, R. (eds.), *Encyclopedia of Iron, Steel, and Their Alloys*. Taylor & Francis, London, in press.
- Nagao, A., Hayashi, K., Oi, K., Mitao, S., 2012b. Effect of uniform distribution of fine cementite on hydrogen embrittlement of low carbon martensitic steel plates. *ISIJ Int.* 52, 213-221.
- Nagao, A., Kuramoto, S., Kanno, M., 1998. Hydrogen microprint technique applied to observe impurity hydrogen in aluminum during deformation. In: Mishra, B. (ed.), *EPD Congress 1998*, TMS, Warrendale, PA, pp. 867-875.
- Nagao, A., Martin, M.L., Dadfarnia, M., Sofronis, P., Robertson, I.M., 2014c. The effect of nanosized (Ti,Mo)C precipitates on hydrogen embrittlement of tempered lath martensitic steel. *Acta Mater.* 74, 244-254.
- Nagao, A., Smith, C.D., Dadfarnia, M., Sofronis, P., Robertson, I.M., 2012a. The role of hydrogen in hydrogen embrittlement fracture of lath martensitic steel. *Acta Mater.* 60, 5182-5189.
- Nagao, A., Smith, C.D., Dadfarnia, M., Sofronis, P., Robertson, I.M. 2014a. Interpretation of hydrogen-induced fracture surface morphologies for lath martensitic steel. *Procedia Mater. Sci.* 3, 1700-1705.
- Nagao, A., Smith, C.D., Martin, M.L., Dadfarnia, M., Sofronis, P., Robertson, I.M. 2014b. The role of plasticity in hydrogen embrittlement fracture of lath martensitic steel. In: Tsuzaki, K., Ohmura, T., Tsuji, N. (Eds.), *The 4th International Symposium on Steel Science*. The Iron and Steel Institute of Japan, Tokyo, pp. 87-90.
- Nagumo, M., Matsuda, H., 2002. Function of hydrogen in intergranular fracture of martensitic steels. *Phil. Mag.* 82, 3415-3425.

- Narita, K., 1975. Physical chemistry of the groups IVa (Ti, Zr), Va (V, Nb, Ta) and the rare earth elements in steel. *Trans. Iron Steel Inst. Japan* 15, 145-152.
- Nelson, H.G., Stein, J.E., 1973. Gas-phase hydrogen permeation through alpha iron, 4130 steel, and 304 stainless steel from less than 100°C to near 600°C. NASA Technical Note NASA TN D-7265, Washington, DC.
- Novak, P., Yuan, R., Somerday, B.P., Sofronis, P., Ritchie, R.O., 2010. A statistical, physical-based, micro-mechanical model of hydrogen-induced intergranular fracture in steel. *J. Mech. Phys. Solids* 58, 206-226.
- Oriani, R.A., 1970. The diffusion and trapping of hydrogen in steel. *Acta Metall.* 18, 147-157.
- Oriani, R.A., 1987. Hydrogen the versatile embrittler. *Corrosion* 43, 390-397.
- Oriani, R.A., Josephic, P.H., 1974. Equilibrium aspects of hydrogen-induced cracking of steels. *Acta Metall.* 22, 1065-1074.
- Oriani, R.A., Josephic, P.H., 1977. Equilibrium and kinetic studies of hydrogen-assisted cracking of steel. *Acta Metall.* 25, 979-988.
- Ouchi, C., Sampei, T., Kozasu, I., 1982. The effect of hot rolling condition and chemical composition on the onset temperature of γ - α transformation after hot rolling. *Trans. Iron Steel Inst. Japan* 22, 214-222.
- Rice, J.R., Wang, J.-S., 1989. Embrittlement of interfaces by solute segregation. *Mater. Sci. Eng. A* 107, 23-40.
- Robertson, I.M., 1999. The effect of hydrogen on dislocation dynamics. *Eng. Fract. Mech.* 64, 649-673.
- Robertson, I.M., Birnbaum, H.K., Sofronis, P., 2009. Hydrogen effects on plasticity. In: Hirth, J.P., Kubin, L. (Eds.), *Dislocations in solids*, vol. 15. Elsevier, Amsterdam, pp. 249-293.
- Saka, H., Imura, T., 1972. Direct measurement of mobility of edge and screw dislocations in 3% silicon-iron by high voltage transmission electron microscopy. *J. Phys. Soc. Japan* 32, 702-716.
- San Marchi, C., Somerday, B.P., Robinson, S.L., 2007. Permeability, solubility and diffusivity of hydrogen isotopes in stainless steels at high gas pressures. *Int. J. Hydrogen Energy* 32, 100-116.

- Scully, J.R., Van Den Avyle, J.A., Cieslak, M.J., Romig Jr., A.D., Hills, C.R., 1991. The influence of palladium on the hydrogen-assisted cracking resistance of PH 13-8 Mo stainless steel. *Metall. Trans. A* 22A, 2429-2444.
- Serra, E., Perujo, A., Benamati, G., 1997. Influence of traps on the deuterium behaviour in the low activation martensitic steels F82H and Batman. *J. Nucl. Mater.* 245, 108-114.
- Shibata, A., Matsuoka, T., Ueno, A., Tsuji, N., 2017. Fracture surface topography analysis of the hydrogen-related fracture propagation process in martensitic steel. *Int. J. Fract.* 205, 73-82.
- Smith, E., 1966. The nucleation and growth of cleavage microcracks in mild steel. In: Stickland, A.C. (Ed.), *Physical Basis of Yield and Fracture*. Institute of Physics and Physical Society, Oxford, pp. 36-46.
- Sofronis, P., Birnbaum, H.K., 1995. Mechanics of the hydrogen-dislocation-impurity interactions—I. increasing shear modulus. *J. Mech. Phys. Solids* 43, 49-90.
- Sofronis, P., Liang, Y., Aravas, N., 2001. Hydrogen induced shear localization of the plastic flow in metals and alloys. *Eur. J. Mech. A – Solids* 20, 857-872.
- Sofronis, P., McMeeking, R.M., 1989. Numerical analysis of hydrogen transport near a blunting crack tip. *J. Mech. Phys. Solids* 37, 317-350.
- Sofronis, P., Taha, A., 2000. Micromechanical modeling of hydrogen transport—a review. In: Kane, R.D. (Ed.), *Environmentally Assisted Cracking: Predictive Models for Risk Assessment and Evaluation of Materials, Equipment, and Structures*. ASTM STP 1401, West Conshohocken, PA, pp. 70-103.
- Somerday, B.P., Sofronis, P. (Eds.), 2014. *Hydrogen-materials interactions*. ASM International, Materials Park, OH.
- Sturges, C.M., Miodownik, A.P., 1969. The interaction of hydrogen and dislocations in iron. *Acta Metall.* 17, 1197-1207.
- Takahashi, J., Kawakami, K., Kobayashi, Y., Tarui, T., 2010. The first direct observation of hydrogen trapping sites in TiC precipitation-hardening steel through atom probe tomography. *Scr. Mater.* 63, 261-264.
- Takai, K., Abe, N., 2013. Identification of hydrogen desorption peak temperatures, binding

- energies, and occupation ratios at vacancies, dislocations and grain boundaries in iron and steel. In: International Hydrogen Energy Development Forum 2013. Kyushu University, Fukuoka, pp. 29-36.
- Takai, K., Akiyama, E. (Eds.), 2012. Special issue on common bases for hydrogen embrittlement studies. *ISIJ Int.* 52.
- Tien, J.K., Thompson, A.W., Bernstein, I.M., Richards, R.J., 1976. Hydrogen transport by dislocations. *Metall. Trans. A*, 7A, 821-829.
- Troiano, A.R., 1960. The role of hydrogen and other interstitials in the mechanical behavior of metals. *Trans. ASM* 52, 54-80.
- Ueji, R., Tsuji, N., Minamino, Y., Koizumi, Y., 2002. Ultragrain refinement of plain low carbon steel by cold-rolling and annealing of martensite. *Acta Mater.* 50, 4177-4189.
- Wang, S., Martin, M.L., Robertson, I.M., Sofronis, P., 2016. Effect of hydrogen environment on the separation of Fe grain boundaries. *Acta Mater.* 107, 279-288.
- Wei, F.G., Hara, T., Tsuzaki, K., 2004. Precise determination of the activation energy for desorption of hydrogen in two Ti-added steels by a single thermal-desorption spectrum. *Metall. Mater. Trans. B* 35B, 587-597.
- Wei, F.G., Tsuzaki, K., 2004. Hydrogen absorption of incoherent TiC particles in iron from environment at high temperatures. *Metall. Mater. Trans. A* 35A, 3155-3163.
- Wei, F.G., Tsuzaki, K., 2006. Quantitative analysis on hydrogen trapping of TiC particles in steel. *Metall. Mater. Trans. A* 37A, 331-353.
- Williamson, G.K., Hall, W.H., 1953. X-ray line broadening from fcc aluminium and wolfram. *Acta Metall.* 1, 22-31.
- Williamson, G.K., Smallman, R.E., 1956. Dislocation densities in some annealed and cold-worked metals from measurements on the X-ray debye-scherrer spectrum. *Phil. Mag.* 1, 34-46.
- Yoshino, K., McMahon Jr., C.J., 1974. The cooperative relation between temper embrittlement and hydrogen embrittlement in a high strength steel. *Metall. Trans.* 5, 363-370.

Table captions

Table 1. Steel chemical composition (mass %) and calculated transformation temperatures.

Table 2. Steel tempering conditions and four-point bending test conditions.

Table 3. Uniaxial tensile properties of steels investigated.

Table 4. Peak 1 hydrogen content, desorption rate peak temperature, and nominal stress at fracture for steels A500, A550 β , B500, and B550.

Table 5. Hydrogen trap binding energies.

Table 6. Calculated lattice and trapped hydrogen concentrations (at. ppm) at room temperature (25°C) prior to loading for baseline steels (steels A500/A550 β) and Ti-added steels (steels B500 and B550) under various charging pressures. The last column shows the concentrations at hydrogen gas charging pressure 138 MPa at temperature 250°C before cooling the steels to room temperature.

Table 7. Material properties and parameters used in the simulations.

Figure Captions

Fig. 1. Schematic illustration of rolling and heat treatment employed.

Fig. 2. Dimensions of a single-edge notch bend specimen in millimeters.

Fig. 3. Microstructure of the Ti-added steel (steel B550): (a) optical image, Nital etched; (b) optical image, picric acid etched; (c) IPF map; (d) image quality map; (e) bright-field electron micrograph showing the overall microstructure; (f) SEM image, Nital etched; (g) bright-field electron micrograph showing the nanosized precipitates marked with arrows; (h) an example of EDX spectrum of the matrix observed in (g); (i) an example of EDX spectrum on the nanosized precipitates shown with arrows in (g). Arrows in (e) and (f) mark cementite particles at lath boundaries. Arrowheads in (e) and (f) indicate cementite particles within laths.

Fig. 4. Statistical information for the microstructure of the Ti-added steel (steel B550): (a) prior austenite grain size; (b) packet size; (c) block width; (d) lath width; (e) cementite particle size; (f) (Ti,Mo)C precipitate size; (g) extracted residue analysis result; (h) Williamson-Hall plots; (i) dislocation densities as a function of strain.

Fig. 5. Nominal stress-strain and true stress-strain curves of the uncharged Ti-added steel (steel B550).

Fig. 6. (a) Thermal desorption analysis spectra from uncharged and hydrogen-charged Ti-added steel (Steel B550) in 31 and 138 MPa hydrogen gas; heating rate = 200 °C/h. (b) Nominal bending stress-displacement curves of four-point bend tests of the uncharged and hydrogen-charged Ti-added steel (B550) for gas pressures of 31 and 138 MPa and a displacement rate 0.1 $\mu\text{m/s}$. (c) Variation in nominal stress at fracture (maximum nominal bending stress) of the uncharged and hydrogen-charged baseline steels (A500 and A550 β) and Ti-added steel (B550) with peak 1 hydrogen content: \circ steel A500, uncharged; \diamond steel A550 β , uncharged; \square steel B550, uncharged; \bullet steel A500, H-charged; \blacklozenge steel A550 β , H-charged; \blacksquare steel B550, H-charged; displacement rate = 0.1 $\mu\text{m/s}$. (Nagao *et al.*, 2014c)

Fig. 7. Variation of the nominal stress at fracture (maximum nominal bending stress) of the Ti-added steel (steel B600) with displacement rate in the absence and presence of hydrogen: \bullet steel

B600, uncharged; ■ steel B600, H-charged in 138 MPa hydrogen gas.

Fig. 8. SEM images close to the notch root of interrupted single-notched specimens of the baseline steel (steel A550) at the onset of fracture: (a) and (b) strain-controlled fracture in the absence of hydrogen initiating directly at the notch root in an uncharged specimen; (c) and (d) stress-controlled fracture in the presence of hydrogen initiating ahead of the notch root in a hydrogen-charged specimen in 138 MPa hydrogen gas. (b) and (d) are higher magnification SEM images of the boxed regions presented in (a) and (c), respectively. Cracks are shown with arrows in (b) and (d).

Fig. 9. SEM images of the fracture surfaces of ruptured four-point bend specimens of the baseline steel (steel A500) and Ti-added steel (steel B550): (a) “flat” intergranular feature of the hydrogen-charged steel A500 exposed to 31 MPa hydrogen gas; (b) “quasi-cleavage” feature of the hydrogen-charged steel A500 exposed to 31 MPa hydrogen gas; (c) ductile microvoid coalescence feature of the uncharged steel B550; (d) mixture of “quasi-cleavage” and ductile microvoid coalescence features of the fracture of the hydrogen-charged steel B550 exposed to 31 MPa hydrogen gas; (e) “quasi-cleavage” feature of fracture in the hydrogen-charged steel B550 exposed to 138 MPa hydrogen gas; (f) higher-resolution image of (e). IG, “QC” and MVC denote intergranular, “quasi-cleavage,” and ductile microvoid coalescence, respectively. Arrows in (a) delineate the fine tear ridges. Arrows and arrowheads in (b) and (d-f) indicate the fine serrated markings and secondary cracks, respectively.

Fig. 10. Possible mechanistic steps in the generation of hydrogen-induced intergranular and “quasi-cleavage” failures of a lath martensitic steel.

Fig. 11. Finite-element mesh lay out for the single-edge notch bend specimen.

Fig. 12. Finite element results showing contour plots at the moment of specimen failure: (a,b) normalized maximum principal stress; (c,d) normalized effective stress; (e,f) normalized concentration of hydrogen trapped at dislocations; (g,h) fraction of debonded interfaces. Figures (a,c,e,g) refer to the A500 steel with an initial hydrogen concentration in normal interstitial lattice sites of $C_0 = 1.054$ at. ppm; Figures (b,d,f,h) refer to the B550 steel with an initial hydrogen concentration in normal interstitial lattice sites of $C_0 = 0.1673$ at. ppm. Both steels

were charged in 31 MPa hydrogen gas.

Fig. 13. Model predictions of the normalized nominal stress σ_{nom} / σ_0 at fracture for different values of hydrogen gas pressure for (a) baseline steels (A500 and A550 β), (b) Ti-added steel (B500) and (c) Ti-added steel (B550). The experimental data for the uncharged and hydrogen-charged steels at 31 or 138 MPa hydrogen gas are superposed on the figure.

Fig. 14. SEM images of (a) the microstructure of an as-quenched lath martensitic steel, Nital etching; (b) hydrogen-induced “flat” intergranular fracture surface; (c) hydrogen-caused “quasi-cleavage” fracture surface.

Table 1. Steel chemical composition (mass %) and calculated transformation temperatures.

Steel	C	Si	Mn	P	S	Mo	Ti	Al soluble	Total N	A_{c1} ¹ (°C)	A_{r3} ² (°C)	M_s ³ (°C)
A (Baseline)	0.401	0.26	1.91	0.005	0.0006	0.23	0.000	0.025	0.0043	710	619	303
B (Ti-added)	0.406	0.26	1.90	0.005	0.0007	0.22	0.041	0.023	0.0049	710	619	301

¹ temperature when austenite begins to form on heating $A_{c1} = 723 - 10.7\text{Mn} - 16.9\text{Ni} + 29.1\text{Si} + 16.9\text{Cr} + 290\text{As} + 6.38\text{W}$.

² temperature when austenite begins to transform to ferrite on cooling $A_{r3} = 910 - 310\text{C} - 80\text{Mn} - 20\text{Cu} - 15\text{Cr} - 55\text{Ni} - 80\text{Mo} + 0.35(t-8)$, where t is the plate thickness (mm).

³ Martensite-start temperature, $M_s = 561 - 474\text{C} - 33\text{Mn} - 17\text{Cr} - 17\text{Ni} - 21\text{Mo}$.

Table 2. Steel tempering conditions and the four-point bending test conditions.

Steel	Tempering conditions			Four-point bending test conditions				Purpose
	Heating rate (°C/s)	Tempering temperature (°C)	Time (min)	Uncharged ($\mu\text{m/s}$)	31 MPa H-charged ($\mu\text{m/s}$)	138 MPa H-charged ($\mu\text{m/s}$)	Ruptured/ Interrupted	
A500 (Baseline)	0.4	500	0	0.1	0.1	0.1	Ruptured	Numerical simulation
A550 α (Baseline)	0.5	550	0	0.1	—	0.1	Interrupted	Critical local fracture event
A550 β (Baseline)	1.9	550	0	0.1	0.1	0.1	Ruptured	Numerical simulation
B500 (Ti-added)	0.5	500	60	0.1	0.1	0.1	Ruptured	Numerical simulation
B550 (Ti-added)	0.6	550	60	0.1	0.1	0.1	Ruptured	Numerical simulation
B600 (Ti-added)	0.7	600	60	0.1, 1.0, 10.0	—	0.1, 1.0, 10.0	Ruptured	Rate effect

Table 3. Uniaxial ensile properties of the steels investigated.

Steel	0.2% Proof stress (MPa)	Ultimate tensile strength (MPa)	Total elongation (%)	Reduction in area (%)
A500 (Baseline)	1010	1195	16.0	40.6
A550 α (Baseline)	990	1096	15.0	35.1
A550 β (Baseline)	1170	1286	12.5	42.8
B500 (Ti-added)	1130	1213	13.5	41.5
B550 (Ti-added)	1090	1189	12.0	30.6
B600 (Ti-added)	1050	1116	15.0	37.7

Table 4. Peak 1 hydrogen content, desorption rate peak temperature, and nominal stress at fracture of the A500, A550 α , A550 β , B500, B550 and B600 steels.

Steel	Hydrogen gas pressure (MPa)	Charging temperature (°C)	Charging duration (days)	Peak 1 hydrogen content		Desorption rate peak temperature (°C)	Nominal stress at fracture (MPa)
				(mass ppm)	(at. ppm)		
A500 (Baseline)	Uncharged	-	-	0.00	0.0	-	2154 ⁴
	31	250	21	0.51	28.4	170	575 ⁴
	138	250	21	0.77	42.8	169	881 ⁴
A550 α (Baseline)	Uncharged	-	-	-	-	-	2044 ⁴
	138	250	21	0.79	44.1	156	855 ⁴
A550 β (Baseline)	Uncharged	-	-	0.00	0.0	-	2289 ⁴
	31	250	21	0.44	24.6	169	480 ⁴
	138	250	21	0.74	41.0	170	725 ⁴
B500 (Ti-added)	Uncharged	-	-	-	-	-	2196 ⁴
	31	250	21	0.71	39.5	170	931 ⁴
	138	250	21	1.59	88.6	184	663 ⁴
B550 (Ti-added)	Uncharged	-	-	0.00	0.0	-	2128 ⁴
	31	250	21	0.82	45.9	194	1260 ⁴
	138	250	21	2.13	118.6	190	618 ⁴
B600 (Ti-added)	Uncharged	-	-	0.01	0.8	-	2100 ⁴
						-	2135 ⁵
						-	2187 ⁶
	138	250	21	3.12	174.0	182	730 ⁴
							1454 ⁵
							1875 ⁶

Displacement rate : ⁴ 0.1 $\mu\text{m/s}$; ⁵ 1.0 $\mu\text{m/s}$; ⁶ 10.0 $\mu\text{m/s}$

Table 5. Hydrogen trap binding energies.

Hydrogen trap state		Hydrogen trap binding energy reported in the literature (kJ/mol)	Hydrogen trap binding energy of this study (kJ/mol)
High-angle grain boundary	Prior austenite grain boundary	<u>47.4</u> ⁷ (Takai and Abe, 2013)	57.4
	Packet boundary		
	Block boundary		
Lath boundary	Edge and screw dislocations	<u>26.0</u> ⁸ 16.7-36.4 (Sturges and Miodownik, 1969; Oriani, 1970; Hirth, 1980; Choo and Lee, 1982; Novak <i>et al.</i> , 2010)	25.7
Dislocation	Cores of screw dislocation	<u>26.0</u> ⁸ 24.7, 37.6 (Itakura <i>et al.</i> , 2013)	25.7
Cementite particle	Incoherent interface	<u>10.9</u> ⁷ (Hong and Lee, 1983b)	14.0
Nanosized (Ti,Mo)C precipitate	Broad interface between (Ti,Mo) platelet and matrix	<u>28.1</u> ⁷ (Lee and Lee, 1984)	30.5

^{7,8} Underlined values were used in the numerical simulations.

⁸ The value was taken between the reported binding energies.

Table 6. Calculated lattice and trapped hydrogen concentrations (in at. ppm) at room temperature (25°C) prior to loading for baseline steels (A500/A550 β) and Ti-added steels (B500 and B550) under various charging pressures. The last column shows the concentrations at hydrogen gas charging pressure 138 MPa at temperature 250°C before cooling the steels to room temperature.

Site	Steel	Hydrogen gas charging pressure					
		1 MPa at 25°C	10 MPa at 25°C	31 MPa at 25°C	80 MPa at 25°C	138 MPa at 25°C	138 MPa at 250°C
Lattice	A500/A550 β	0.00759	0.40130	1.0540	2.1650	3.4070	39.0159
	B500	0.01375	0.09441	0.1981	0.3714	0.5580	39.0159
	B550	0.01545	0.08290	0.1673	0.3082	0.4593	39.0159
High-angle grain boundary	A500/A550 β	3.586	5.837	5.881	5.895	5.900	4.0113
	B500	4.352	5.616	5.765	5.831	5.857	4.0113
	B550	4.482	5.577	5.740	5.815	5.846	4.0113
Dislocation	A500/A550 β	0.00107	0.05575	0.14310	0.28300	0.42760	0.05930
	B500	0.00194	0.01326	0.02773	0.05165	0.07709	0.05930
	B550	0.00218	0.01165	0.02344	0.04295	0.06368	0.05930
Cementite particles	A500/A550 β	0.000219	0.01158	0.03041	0.06244	0.09826	0.1695
	B500	0.000397	0.00272	0.00572	0.01072	0.01610	0.1695
	B550	0.000446	0.00239	0.00483	0.00889	0.01325	0.1695
Lath boundary	A500/A550 β	0.0971	5.060	12.988	25.680	38.805	5.3817
	B500	0.1758	1.203	2.516	4.688	6.996	5.3817
	B550	0.1976	1.057	2.127	3.898	5.779	5.3817
(Ti,Mo)C precipitates	A500/A550 β	—	—	—	—	—	—
	B500	1.982	13.51	28.12	51.97	76.90	41.77
	B550	3.686	19.66	39.40	71.74	105.61	69.13
Total	A500/A550 β	3.692	11.365	20.096	34.085	48.638	48.638
	B500	6.527	20.444	36.632	62.918	90.404	90.404
	B550	8.384	26.392	47.466	81.809	117.768	117.768

Table 7. Material properties and parameters used in the simulations.

Properties	Symbol	Value
Lattice parameter	a	0.2867 nm
Young's modulus	E	200 GPa
Poisson's ratio	ν	0.3
0.2% proof stress	σ_0	1090 MPa
Work hardening exponent	n	0.03
Number of NILS per host atom	β	1
Molar volume of the host lattice	V_M	$7.11 \times 10^{-6} \text{ m}^3/\text{mol}$
Partial molar volume of hydrogen	V_H	$2 \times 10^{-6} \text{ m}^3/\text{mol}$ (Hirth, 1980)
Diffusion coefficient	D	$1.5 \times 10^{-8} \text{ m}^2/\text{s}$ (Nelson and Stein, 1973)
High-angle grain boundary trap binding energy	$W_B^{(GB)}$	47.4 kJ/mol
High-angle grain boundary trap site density	$\alpha^{(GB)} N_T^{(GB)}$	$5.0 \times 10^{23} \text{ sites/m}^3$ (Hirth, 1980)
Lath boundary trap binding energy	$W_B^{(LB)}$	26.0 kJ/mol
Lath boundary trap site density	$\alpha^{(LB)} N_T^{(LB)}$	$3.0 \times 10^{25} \text{ sites/m}^3$
Dislocation trap binding energy	$W_B^{(D)}$	26.0 kJ/mol
Number of trap sites per dislocation	$\alpha^{(D)}$	1
Dislocation trap density ⁹	$N_T^{(D)}$	$= \sqrt{2}\rho / a$ (See Appendix B) ρ = dislocation density
Cementite particle trap binding energy	$W_B^{(C)}$	10.9 kJ/mol
Cementite particle trap site density	$\alpha^{(C)} N_T^{(C)}$	$3.0 \times 10^{25} \text{ sites/m}^3$
(Ti,Mo)C precipitate trap binding energy	$W_B^{(Ti)}$	28.1 kJ/mol
(Ti,Mo)C precipitate trap site density (steel B500)	$\alpha^{(Ti)} N_T^{(Ti)}$	$1.45 \times 10^{26} \text{ sites/m}^3$
(Ti,Mo)C precipitate trap site density (steel B550)	$\alpha^{(Ti)} N_T^{(Ti)}$	$2.4 \times 10^{26} \text{ sites/m}^3$

⁹ The dislocation trap density, $N_T^{(D)}$ equals to $3.31 \times 10^{23} \text{ traps/m}^3$ for the unstrained lattice, increases linearly with plastic strain, and saturates at $N_T^{(D)} = 1.13 \times 10^{25} \text{ traps/m}^3$ at a plastic strain of 1.9%.

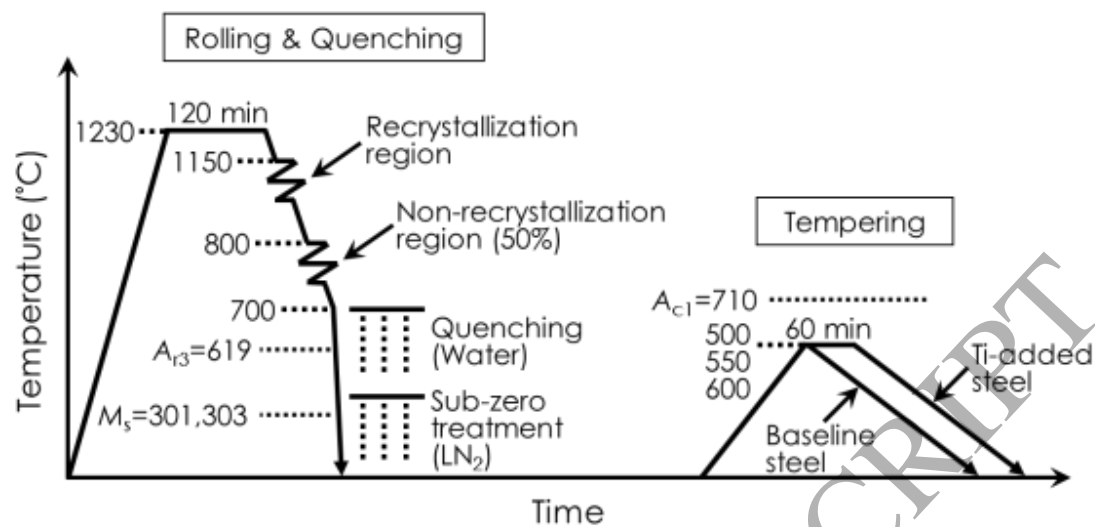


Fig. 1. Schematic illustration of rolling and heat treatment employed.

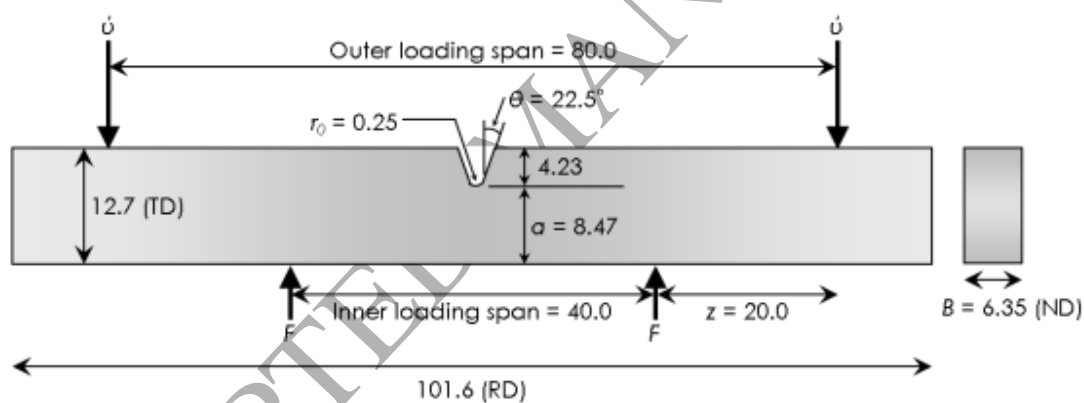


Fig. 2. Dimensions of a single-edge notch bend specimen in millimeters.

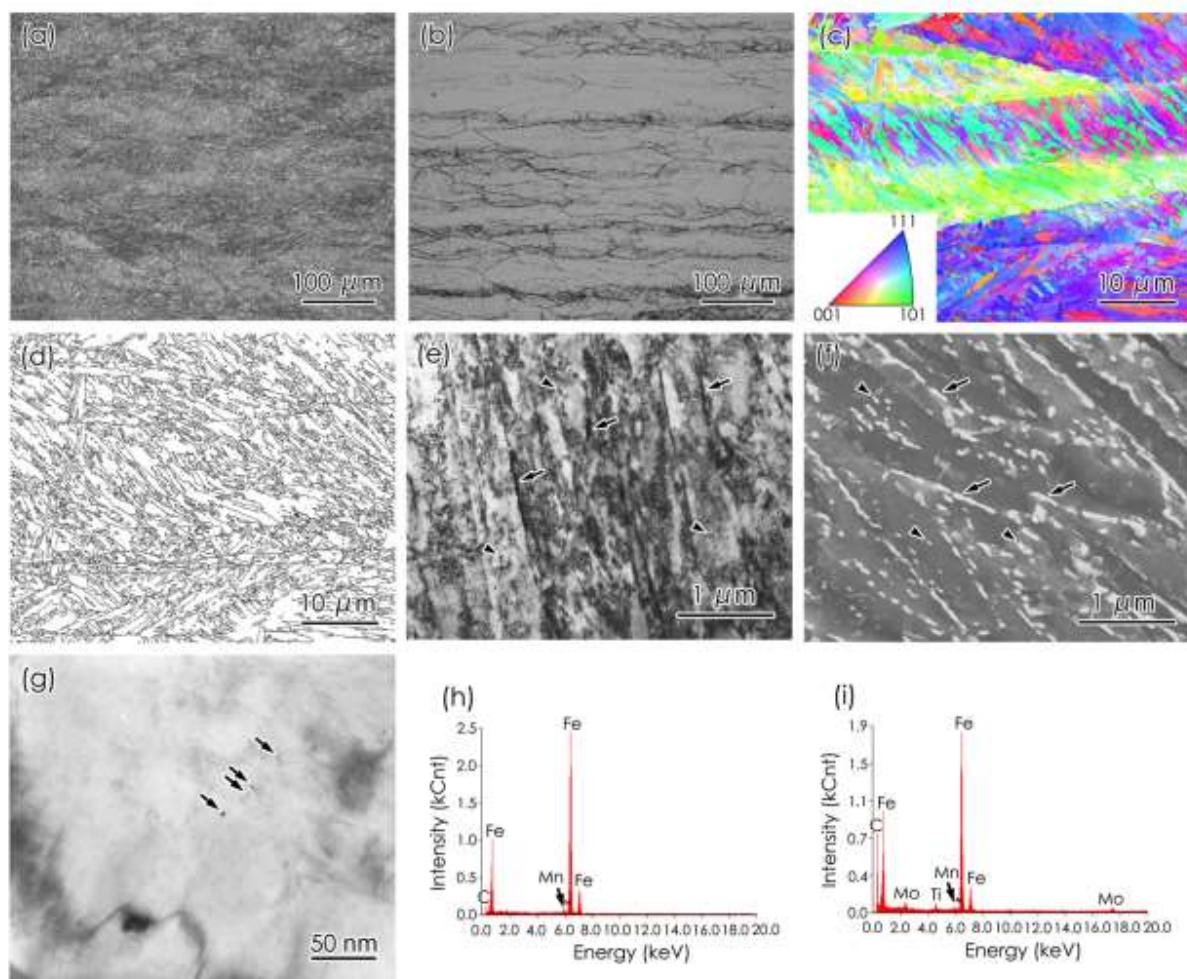


Fig. 3. Microstructure of the Ti-added steel (steel B550): (a) optical image, Nital etched; (b) optical image, picric acid etched; (c) IPF map; (d) image quality map; (e) bright-field electron micrograph showing the overall microstructure; (f) SEM image, Nital etched; (g) bright-field electron micrograph showing the nanosized precipitates marked with arrows; (h) an example of EDX spectrum of the matrix observed in (g); (i) an example of EDX spectrum on the nanosized precipitates shown with arrows in (g). Arrows in (e) and (f) mark cementite particles at lath boundaries. Arrowheads in (e) and (f) indicate cementite particles within laths.

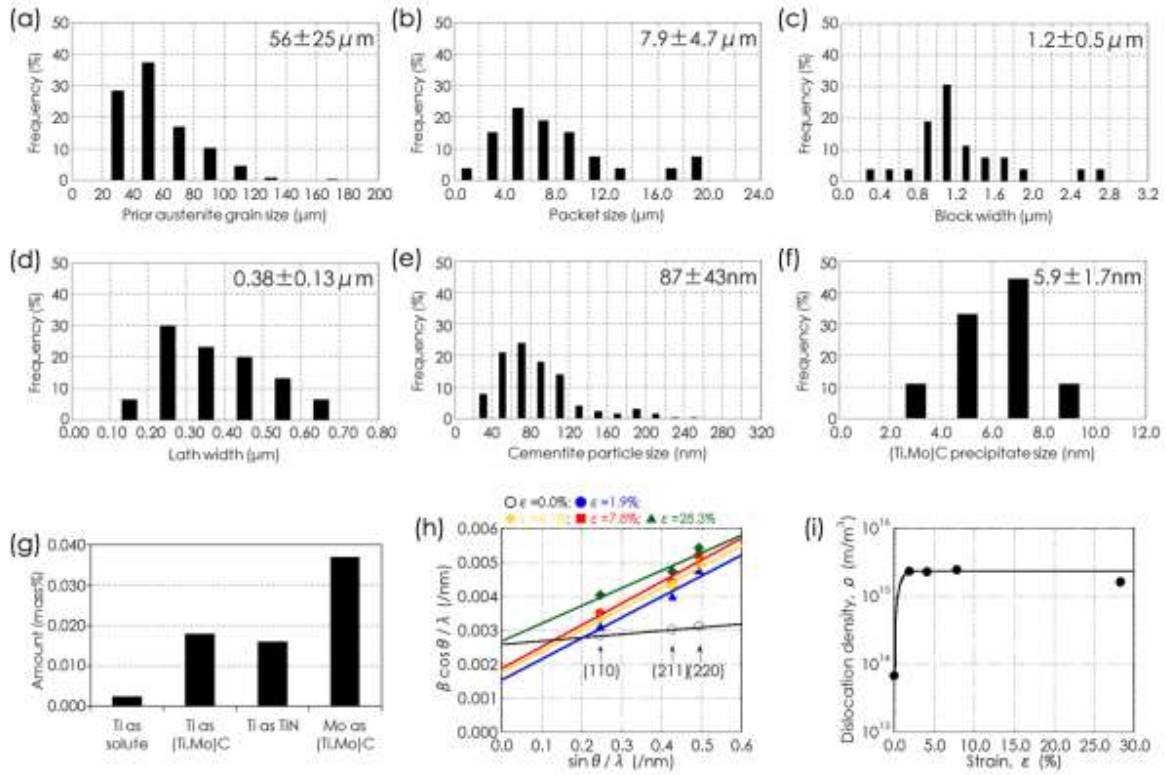


Fig. 4. Statistical information for the microstructure of the Ti-added steel (steel B550): (a) prior austenite grain size; (b) packet size; (c) block width; (d) lath width; (e) cementite particle size; (f) (Ti,Mo)C precipitate size; (g) extracted residue analysis result; (h) Williamson-Hall plots; (i) dislocation densities as a function of strain.

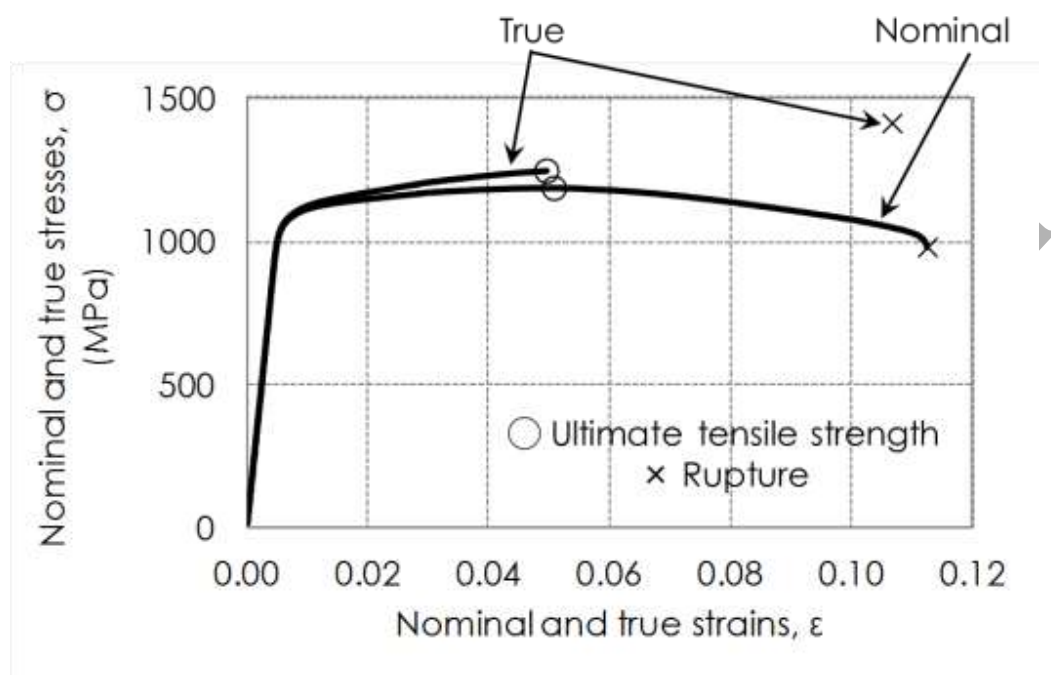


Fig. 5. Nominal stress-strain and true stress-strain curves of the uncharged Ti-added steel (steel B550).

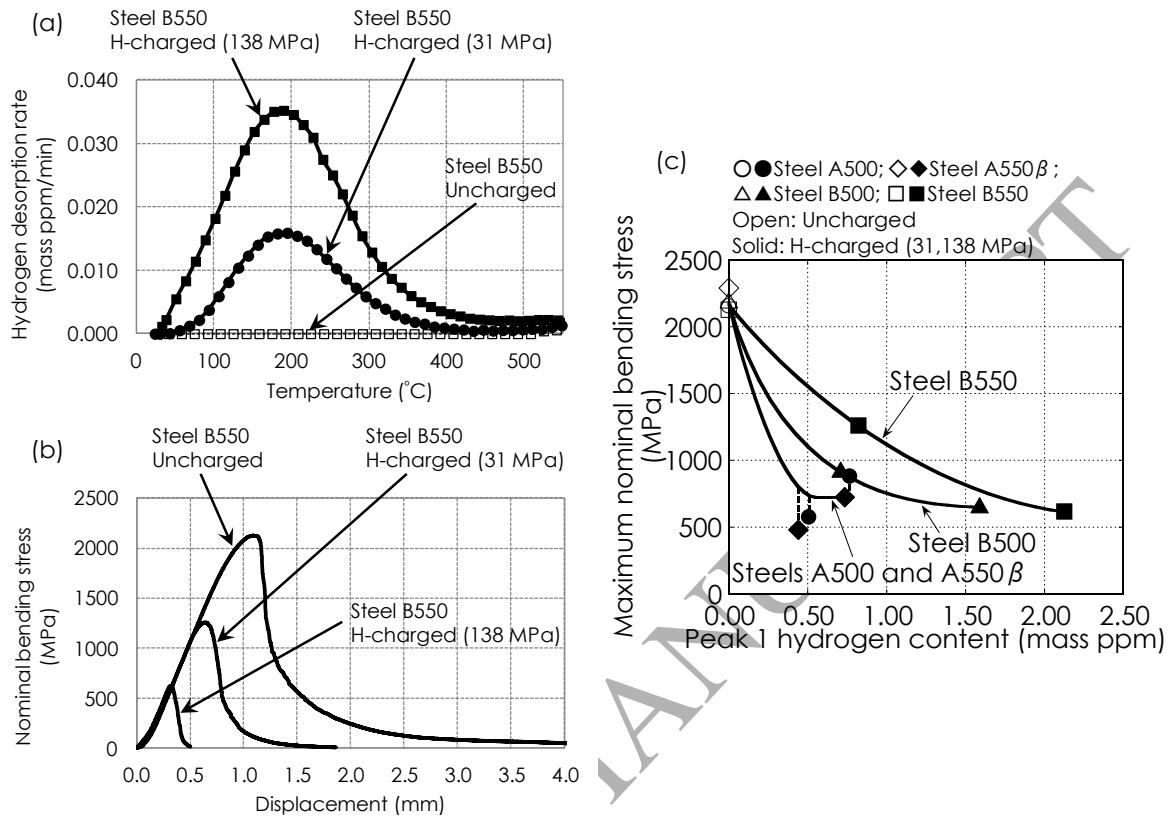


Fig. 6. (a) Thermal desorption analysis spectra from uncharged and hydrogen-charged Ti-added steel (steel B550) in 31 and 138 MPa hydrogen gas; heating rate = 200 °C/h. (b) Nominal bending stress-displacement curves of four-point bend tests of the uncharged and hydrogen-charged Ti-added steel (B550) for gas pressures of 31 and 138 MPa and a displacement rate 0.1 $\mu\text{m/s}$. (c) Variation in nominal stress at fracture (maximum nominal bending stress) of the uncharged and hydrogen-charged baseline steels (A500 and A550 β) and Ti-added steel (B550) with peak 1 hydrogen content: \circ steel A500, uncharged; \diamond steel A550 β , uncharged; \square steel B550, uncharged; \bullet steel A500, H-charged; \blacklozenge steel A550 β , H-charged; \blacksquare steel B550, H-charged; displacement rate = 0.1 $\mu\text{m/s}$. (Nagao *et al.*, 2014c)

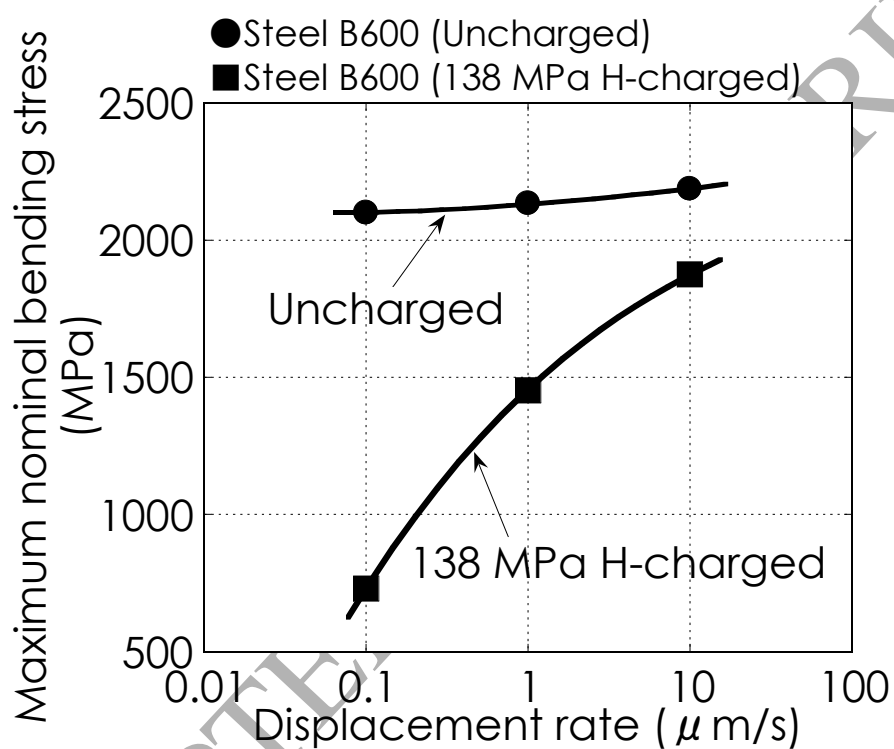


Fig. 7. Variation of the nominal stress at fracture (maximum nominal bending stress) of the Ti-added steel (steel B600) with displacement rate in the absence and presence of hydrogen: ● steel B600, uncharged; ■ steel B600, H-charged in 138 MPa hydrogen gas.

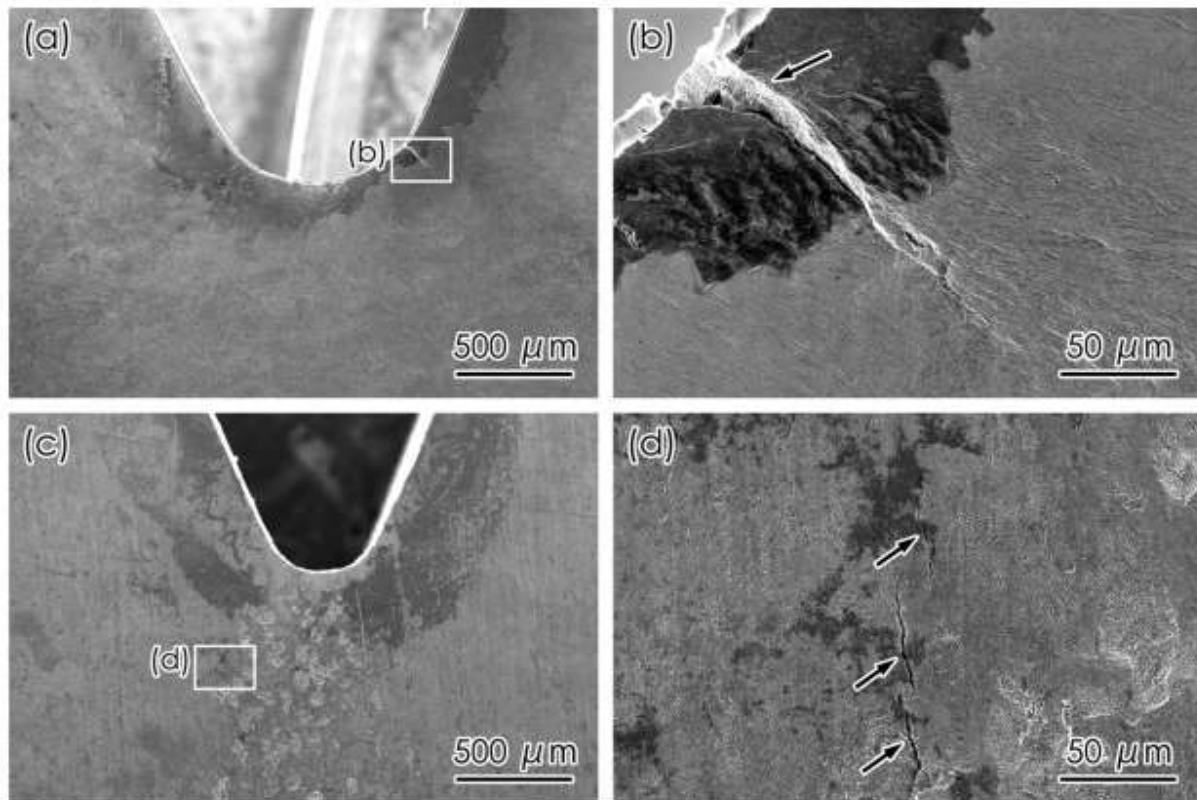


Fig. 8. SEM images close to the notch root of interrupted single-notched specimens of the baseline steel (steel A550) at the onset of fracture: (a) and (b) strain-controlled fracture in the absence of hydrogen initiating directly at the notch root in an uncharged specimen; (c) and (d) stress-controlled fracture in the presence of hydrogen initiating ahead of the notch root in a hydrogen-charged specimen in 138 MPa hydrogen gas. (b) and (d) are higher magnification SEM images of the boxed regions presented in (a) and (c), respectively. Cracks are shown with arrows in (b) and (d).

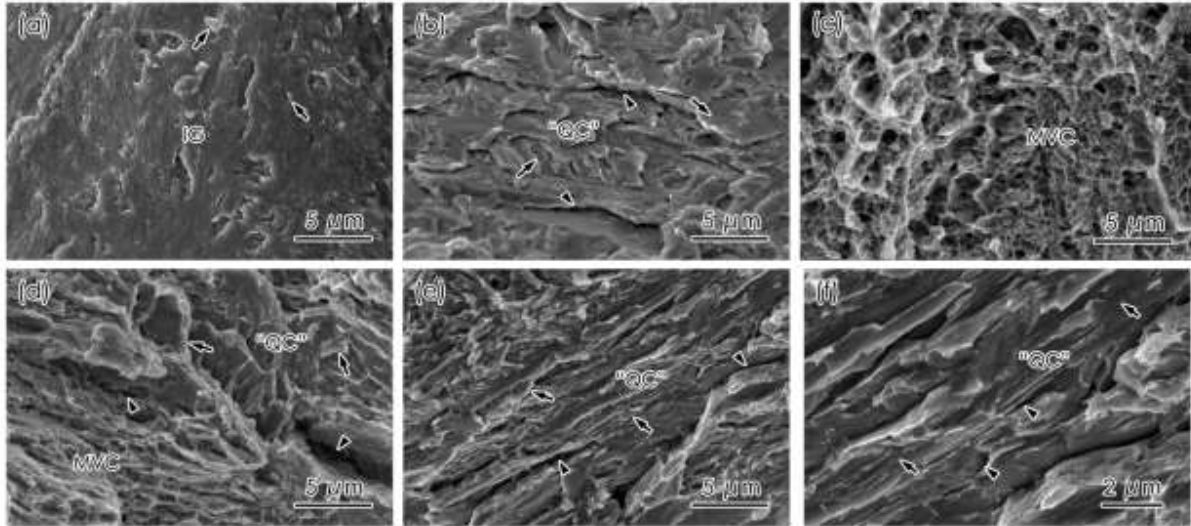


Fig. 9. SEM images of the fracture surfaces of ruptured four-point bend specimens of the baseline steel (steel A500) and Ti-added steel (steel B550): (a) “flat” intergranular feature of the hydrogen-charged steel A500 exposed to 31 MPa hydrogen gas; (b) “quasi-cleavage” feature of the hydrogen-charged steel A500 exposed to 31 MPa hydrogen gas; (c) ductile microvoid coalescence feature of the uncharged steel B550; (d) mixture of “quasi-cleavage” and ductile microvoid coalescence features of the fracture of the hydrogen-charged steel B550 exposed to 31 MPa hydrogen gas; (e) “quasi-cleavage” feature of fracture in the hydrogen-charged steel B550 exposed to 138 MPa hydrogen gas; (f) higher-resolution image of (e). IG, “QC” and MVC denote intergranular, “quasi-cleavage,” and ductile microvoid coalescence, respectively. Arrows in (a) delineate the fine tear ridges. Arrows and arrowheads in (b) and (d-f) indicate the fine serrated markings and secondary cracks, respectively.

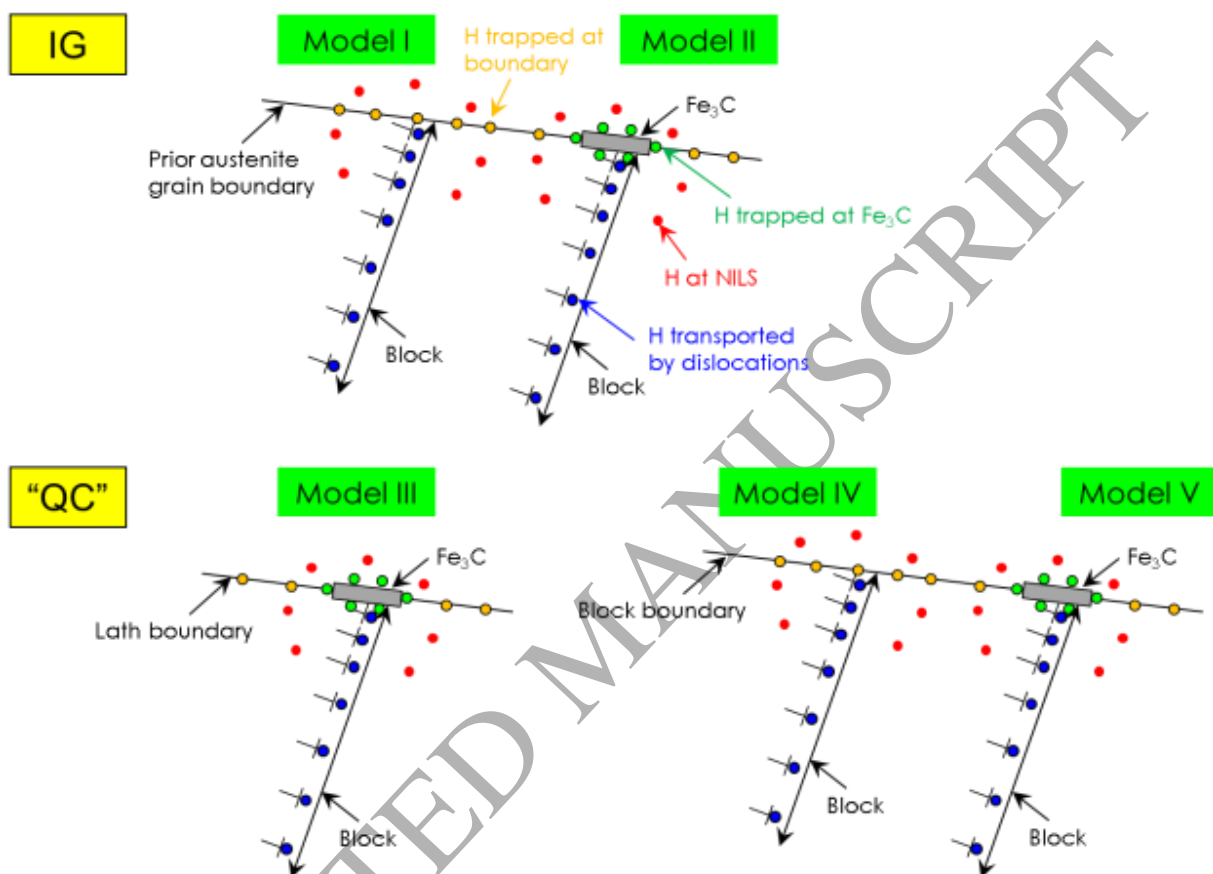


Fig. 10. Possible mechanistic steps in the generation of hydrogen-induced intergranular and “quasi-cleavage” failures of a lath martensitic steel.

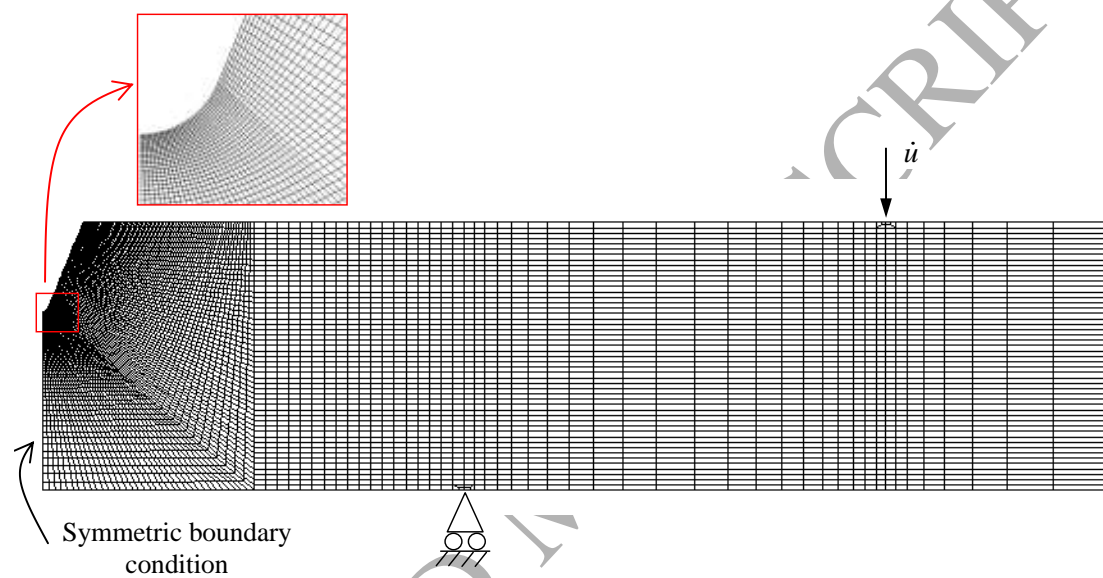
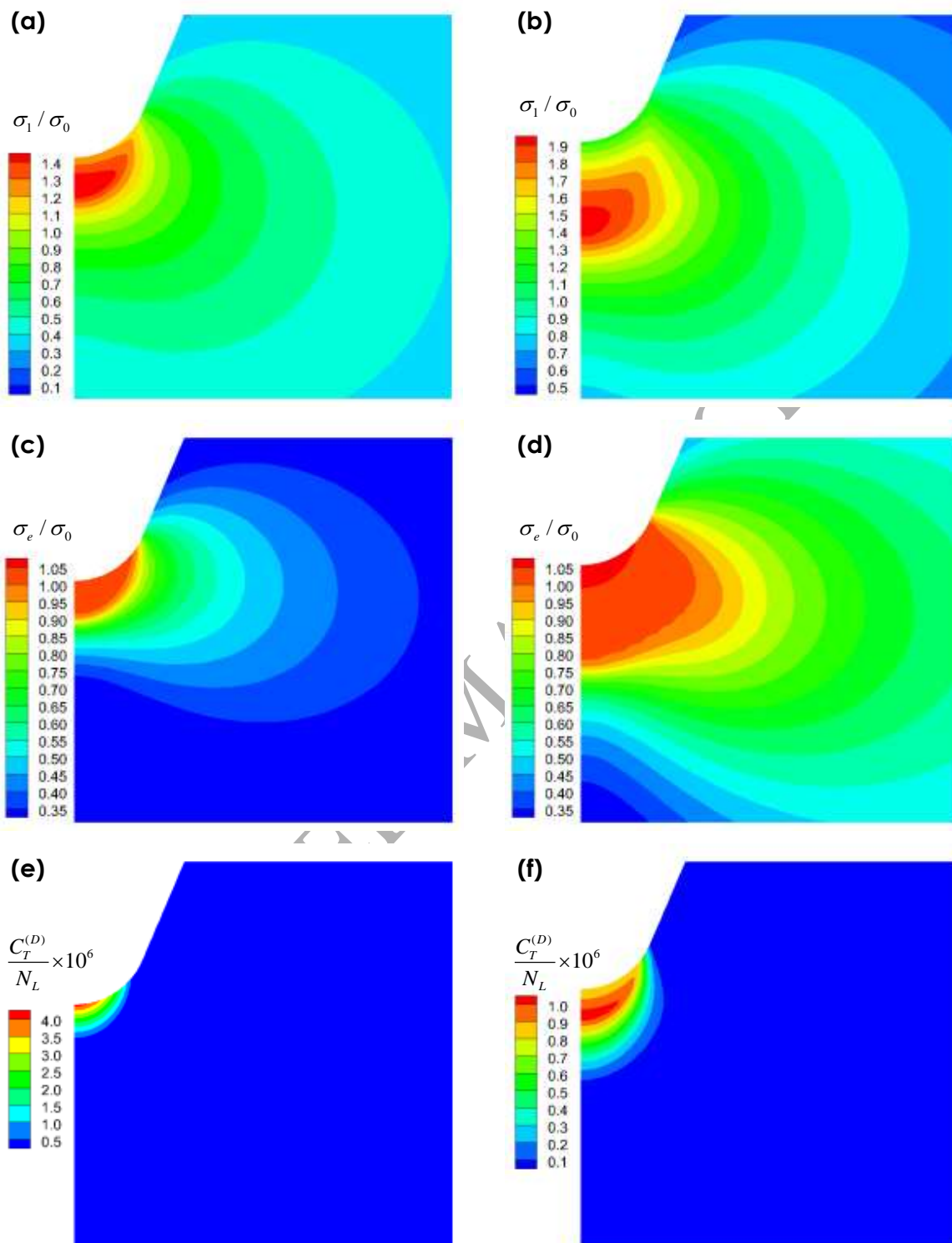


Fig. 11. Finite-element mesh lay out for the single-edge notch bend specimen.



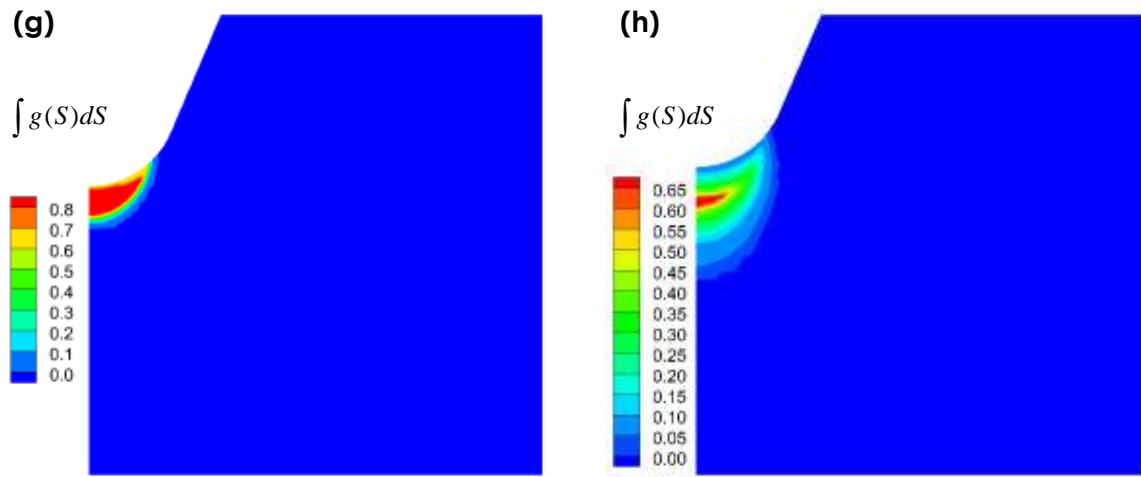
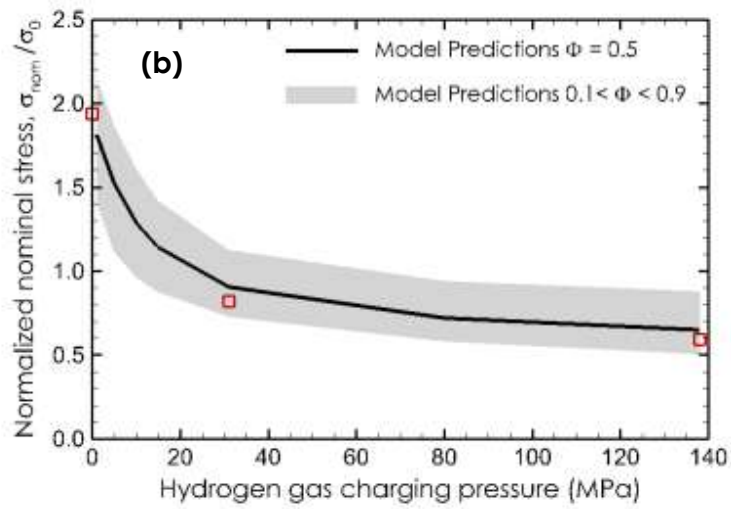
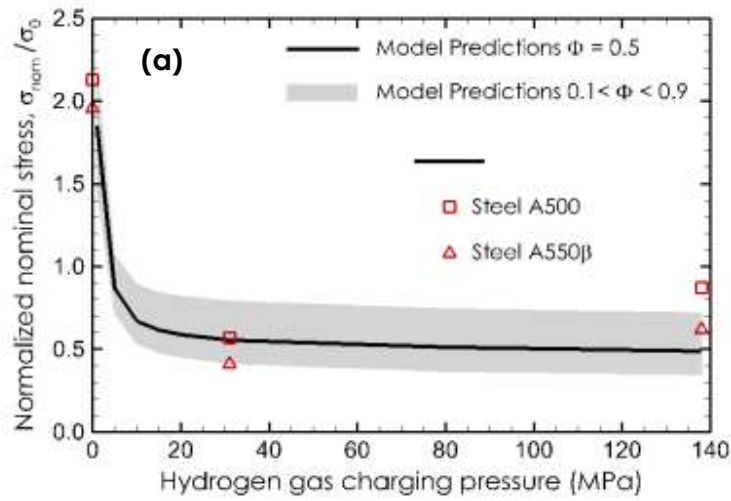


Fig. 12. Finite element results showing contour plots at the moment of specimen failure: (a,b) normalized maximum principal stress; (c,d) normalized effective stress; (e,f) normalized concentration of hydrogen trapped at dislocations; (g,h) fraction of debonded interfaces. Figures (a,c,e,g) refer to the A500 steel with an initial hydrogen concentration in normal interstitial lattice sites of $C_0 = 1.054$ at. ppm; Figures (b,d,f,h) refer to the B550 steel with an initial hydrogen concentration in normal interstitial lattice sites of $C_0 = 0.1673$ at. ppm. Both steels were charged in 31 MPa hydrogen gas.



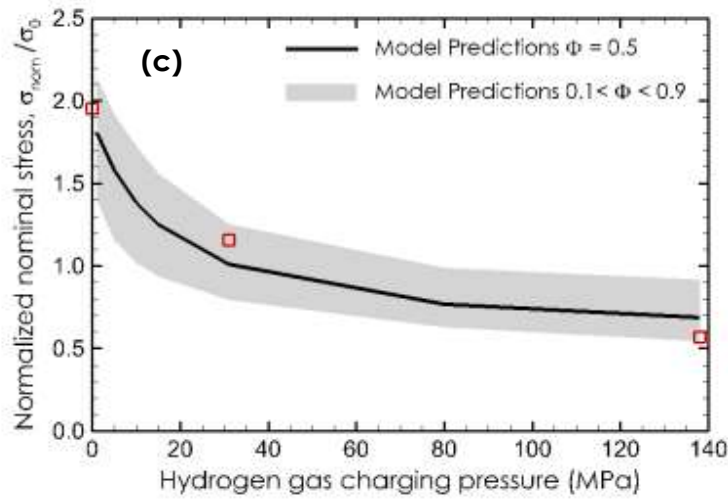


Fig. 13. Model predictions of the normalized nominal stress σ_{nom}/σ_0 at fracture for different values of hydrogen gas pressure for (a) baseline steels (A500 and A550 β), (b) Ti-added steel (B500) and (c) Ti-added steel (B550). The experimental data for the uncharged and hydrogen-charged steels at 31 or 138 MPa hydrogen gas are superposed on the figure.

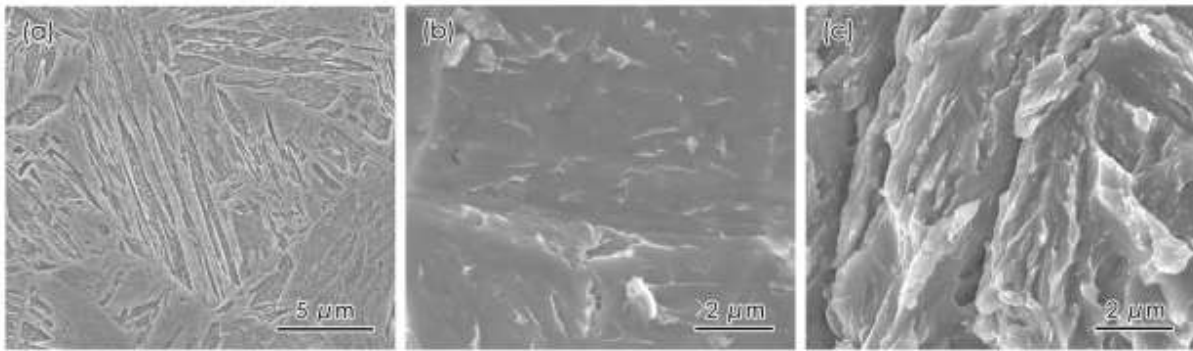


Fig. 14. SEM images of (a) the microstructure of an as-quenched lath martensitic steel, Nital etching; (b) hydrogen-induced “flat” intergranular fracture surface; (c) hydrogen-caused “quasi-cleavage” fracture surface.